Ocean Dynamics

Call for Papers for a Topical Collection on

Multi-scale Modeling of Coastal, Shelf and Global Ocean Dynamics

Evaluation of a Finite-Element Sea-Ice ocean model (FESOM) setup to study the interannual to decadal variability in the deep-water formation rates

P. Scholz · G. Lohmann · Q. Wang · S. Danilov

Received: date / Accepted: date

Abstract The characteristics of a global setup of the Finite-Element Sea-Ice Ocean Model (FESOM) under forcing of the period 1958-2004 are presented. The model setup is designed to study the variability in the deep-water mass formation areas and was therefore regionally better resolved in the deep-water formation areas in the Labrador Sea, Greenland Sea, Weddell Sea and Ross Sea. The sea-ice model reproduces realistic sea-ice distributions and variabilities in the sea ice extent of both hemispheres as well as sea ice transport that compares well with observational data. Based on a comparison between model and Ocean Weather Ship data in the North Atlantic, we observe that the vertical structure is well captured in areas with a high resolution. In our model setup we are able to simulate decadal ocean variability including several salinity anomaly events and corresponding fingerprint in the vertical hydrography. The ocean state of the model setup features pronounced variability in the Atlantic Meridional Overturning Circulation (AMOC) as well as the associated mixed layer depth pattern in the North Atlantic deep-water formation areas.

Keywords Finite-element method · Sea-ice ocean model · COREv2 · Atlantic Meridional Overturning Circulation · Decadal variability

1 Introduction

To challenge the task of future ocean modelling, we need the ability to faithfully resolve coastlines and regional areas of interest without losing the global context of the ocean general circulation. It has been shown, since the early

P. Scholz · G. Lohmann · Q. Wang · S. Danilov
Alfred Wegener Institute for Polar and Marine Research, Bremerhaven, Germany
Tel.: +49(471)4831-1050
E-mail: Patrick.Scholz@awi.de

P. Scholz · G. Lohmann
MARUM, University of Bremen, Bremen, Germany

work of Fix (1975) that the Finite-Element (FE) method in conjunction with an unstructured mesh can be a suitable approach to fulfil this requirement. The FE method provides an easy conservation of energy and a natural treatment of geometric boundaries (Danilov et al, 2004; Wang et al, 2008a; Timmermann et al, 2009). There have been only a few FE ocean general circulation models developed so far that employ the capability of unstructured meshes (Danilov et al, 2004; Ford et al, 2004; White et al, 2008a). In this paper we use the Finite-Element Sea-Ice Ocean Model (FESOM) (Danilov et al, 2004, 2005; Wang et al, 2008b; Timmermann et al, 2009), which is an ocean general circulation model coupled to a dynamic thermodynamic sea-ice model. FESOM uses unstructured triangular meshes, that allow for local refinement in an otherwise global setup. Wang et al (2010) showed that FESOM is able to simulate the tidal impacts on the overflow dynamics and bottom water formation in the Ross Sea. In a global setup, Sidorenko et al (2011) showed that FESOM is able to simulate the large-scale ocean circulation and compared it with other Ocean General Circulation Models (OGCMs) (Griffies et al, 2009). In this paper we show the evaluation of a global FESOM setup, which will be used to model the variability in the deep-water mass formation areas in future work. For this purpose we took the advantage of the unstructured mesh functionality and resolved locally the deep water formation areas in the Labrador Sea, Greenland Sea, Weddell Sea and Ross Sea with higher resolution. For our model-data comparison we make use of sea ice observational fields from Cavalieri et al (1996, updated 2007) and Meier et al (2006, updated 2007). To further validate our model setup and results, we compared the model data with data from ocean weather ships (OWS) (Lazier, 1980; Levitus et al, 1994). The OWS data provide unique long time series in the vertical ocean structure and can be used for estimating ocean hydrography and circulation changes (Haak et al, 2003; Lohmann et al, 2008). For the assessment of the model results we mostly focus on the Atlantic region.

The paper is organized as follows: in section 2 a detailed description of the FESOM model setup and an analysis of the spinup procedure and convergence of the model at the example of the Atlantic Meridional Overturning Circulation (AMOC) is presented. The performance of the sea-ice model is analysed in section 3. In the 4th section of the paper, the ocean model is validated on the basis of a comparison with the ocean weather ship data and the ability of reproducing Great Salinity Anomaly (GSA) events and the Nordic Sea overflow Dickson et al (1988). At the end of this section a Composite Map Analysis of the maximum AMOC index with the meridional AMOC, temperature and salinity profile, as well as with the boreal winter mixed layer depth is used to analyse some first variability that the model generates. The main discussions and conclusions are presented in section 5 and 6, respectively.

2 Model Description

2.1 Global Finite-Element Sea-Ice Ocean Model Setup

The FESOM model, developed at the Alfred Wegner Institute for Polar and Marine Research (Danilov et al, 2004, 2005; Wang et al, 2008b) is a new approach towards simulating the global ocean circulation. The model consists of the Finite-Element ocean model (FEOM) and a Finite-Element dynamic thermodynamic Sea-Ice Model (Timmermann et al, 2009). The current version of FEOM does not differ significantly from the numerical principals described by Wang et al (2008b), except that tetrahedral discretization is used instead of prismatic. FEOM solves the primitive equations under a Boussinesq approximation, by splitting the equations into a dynamical and thermodynamical subsets, which are solved separately to avoid the simultaneous treatment of non-linear dynamics and thermodynamics. The dynamical part consists of solving the momentum equation and the integral continuity equation. The thermodynamical part of the ocean model solves the tracer equations for potential temperature T and salinity S as well as the density ρ which is computed via the equation of state. The ocean model uses a continuous Galerkin formulation, where the primitive equations are discretized with linear continuous basic functions (Danilov et al, 2004). The numerical core of the sea-ice model is described in detail by Timmermann et al (2009).
The setup that we created for our purpose includes an unstructured triangular surface mesh, which is shared by the ocean and sea-ice model. The vertical discretization employs a z level approach, where the mesh nodes are aligned under each other. This prevents difficulties in resolving the hydrostatic balance (Danilov et al, 2004; Sidorenko et al, 2011). The combination of triangular surface mesh and the vertical alignment of nodes under each other creates at first prismatic volumes. Each of this prism is than split into 3 tetrahedral elements on which the model is working.
Fig. 1 shows the approximated mesh resolution used in this paper. The setup is configured on a longitude-latitude mesh, where the latitude coordinate is scaled with $\cos(\Theta)$ to provide a uniform triangular grid in polar areas. The mesh itself is rotated so that the poles are over Greenland and the Antarctic continent. The resulting convergence of the meridians increases the resolution around the coast of Greenland and Antarctica to a minimum value of ~ 7 km and ~ 30 km, respectively. The locally achieved minimum resolution is a trade-off of: i) the global coverage of our setup, ii) the locally increased resolution and iii) the maximum availability of mesh points due to a limitation in computational RAM. The bulk of the model domain has a resolution of $\sim 2^\circ \times 2^\circ \cos(\Theta)$.
To adapt the setup for our special purposes to adequately simulate the deep-water formation, we further increased the resolution in important deep-water formation areas. On the northern hemisphere we increased the resolution to $7 - 20$ km in the Labrador Sea (LS) and to $10 - 20$ km near the Greenland Scotland Ridge. On the Southern Hemisphere, we increased the resolution

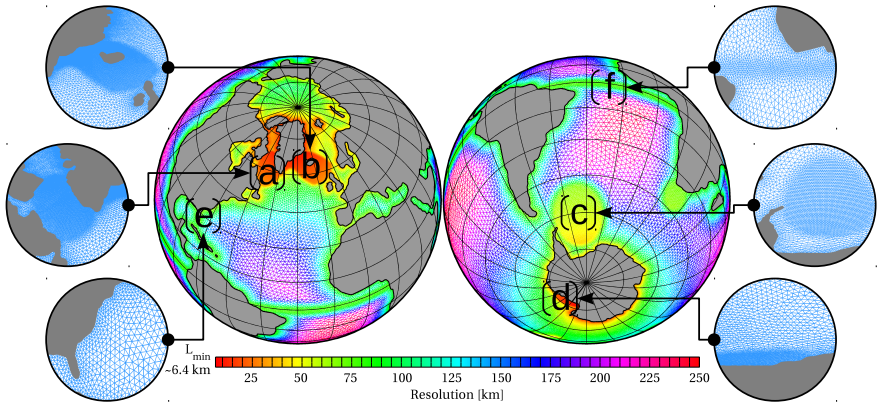

Fig. 1 Global resolution of the model setup and highlighted areas with increased resolution on the northern hemisphere in Labrador Sea (a), Greenland Sea (b) and on the southern hemisphere in Weddell Sea (c) and Ross Sea (d). The resolution in Equatorial (f) and coastal areas (e) is increased as well.

in the central Weddell Sea to $35 - 75$ km and in the Ross Sea with minimum values that are in the order of 10 km. It should be mentioned that the achieved minimum resolution in the Labrador Sea and around the coast of Greenland is still non-eddy resolving. Because coastal and equatorial upwelling regions can also play an important role in driving the large-scale ocean circulation we tried to refine them as well. The coastal resolution is scaled with $S_{min} + (S_{max} - S_{min}) \cdot \tanh(d_i)$, where d_i is the minimum distance of each mesh point to the coast. S_{min} is the resolution at the coast and S_{max} is the resolution in the ocean interior. With this method we reach a globally refined coastal area with a resolution of $50 - 75$ km. Additionally, we refined the mesh in a belt of 10° around the equator with a resolution of 70 km.
A 20 minutes time step is used, determined by the finest resolution in the mesh, because advection and horizontal diffusion are treated explicitly. The bottom topography of the model setup is derived from the ETOPO5 gridded elevation data (Edwards, 1989). We use 41 vertical levels with a vertical resolution of 10 m near the surface and a stepwise increasing maximum layer thickness of 300 m after a depth of 2700 m. Due to the high resolution in critical areas like Denmark Strait, Iceland-Scotland Ridge or Labrador Sea we avoid to artificially deepen the ridges as in standard coarse-resolution models. To prevent the model from a sudden blowing up due to unstable conditions that are created by exceptional high wind forcing we increased the vertical background viscosity ($1 \cdot 10^{-3}$ m^2/s) for the upper three layers by a factor of 3.
For the sea surface forcing we used the data from the Common Ocean-Ice Reference Experiment version 2 (COREv2) (Large and Yeager, 2008). It includes surface air temperature, specific humidity, surface wind speed, radiation flux and precipitation. The implementation of the forcing uses the bulk

formula of Large and Yeager (2008) and includes turbulent fluxes for heat (sensible and latent), water (evaporation), momentum (wind stress), radiative heat fluxes (shortwave and longwave) and water fluxes such as precipitation and river runoff. For the sea surface salinity (SSS) we are using the transient Simple Ocean Data Assimilation (SODA v2.0.3) (Carton and Giese, 2008) salinity data from 1958-2004. The SSS is restored with a piston velocity of 50 m/300 days, similar to Wang et al (2012b) and Sidorenko et al (2011). Sensitivity experiments with different piston velocities (not shown) revealed that the strength of the SSS restoring has a minor influence on the variability of the AMOC. All our simulations were run with a linear free surface.

2.2 Spinup

The model is initialised with temperature and salinity data from the World Ocean Atlas (WOA) (2001). Thereafter the model is run with the combined COREv2 and SODA forcing for the period of 1958-2004 with four repeating cycles to reach a quasi-equilibrium state in the upper and intermediate ocean. The result of the last simulation year (2004) is then taken as the initial condition of the subsequent cycle. Due to the relatively high numerical cost of the FESOM approach, it is not possible to spinup the model for 1000 years (as is the case in other OGCMs) with our present computer resources. The spinup procedure and convergence of the model is analysed in terms of AMOC profiles and maximum AMOC variability at 26°N and 45°N. The calculation of transport quantities (e.g. streamfunction) that require a differentiation or integration of velocity data can cause some problems when we use an unstructured mesh with the FE method. Sidorenko et al (2009) described in detail the common problem of interpreting the data not in a Finite-Element sense when interpolating them to regular meshes. This means that in the Finite-Element sense, mass transport takes place between neighboring nodes of the unstructured mesh, whereas on regular discretisation transport is directed normal to the face of the neighboring boxes. The discrepancy in the direction of the transport between the unstructured and regular discretisation leads to an additional error which manifests itself in an offset of the vertical integral continuity equation of the regular discretisation. The error can be minimized to a certain degree by increasing the resolution of the regular mesh, as shown by Sidorenko et al (2009). They further propose ways in reducing the error when calculating the streamfunction via the horizontal velocities.
Here we use a different approach when calculating the AMOC streamfunction Ψ than Sidorenko et al (2009) and calculate Ψ via the vertical velocity w:

$$\begin{aligned} \frac{d\Psi}{dy} &= \int_{x_W}^{x_E} w(x,y,z)\,dx \\ \Psi(y,z) &= -\int_{y}^{y_S}\left(\int_{x_W}^{x_E} w(x,y',z)\,dx\right)dy' \end{aligned}$$

We find that the interpolation of the vertical velocity from the unstructured FESOM mesh to an regular mesh is much less affected by numerical errors than the meridional velocity. This results in a smoother and less noisy representation of the AMOC and the avoidance of filter algorithms.
The progress of the spinup process of the model is shown in Fig. 2 (a)-(d) in terms of the AMOC, averaged from 1958-2004 for each cycle and the time evolution of the annual maximum AMOC index at 26°N and 45°N (Fig. 2e). The first cycle (Fig. 2a) shows a pronounced upper circulation cell with a maximum value of ~ 10 Sv ($1\ \text{Sv} = 10^6\ \text{m}^3/\text{s}$) and a weakly developed bottom circulation cell with a magnitude of ~ -1 Sv. The inversion layer between the upper and the bottom circulation cell shows a light slope with a mean depth of ~ 3000 m. In the subsequent cycle (Fig. 2b) the magnitude of the upper circulation cell decreases to a value of 9 Sv while the magnitude of bottom cell is slightly increasing and extending more northward. The slope of the boundary between the upper and the bottom cell is decreasing and the mean depth of the upper cell is becoming shallower with a value of ~ 2700 m. In the third spinup cycle (Fig. 2c), the upper circulation cell of the AMOC is still becoming slightly weaker, while the magnitude of the bottom cell further extends to values of ~ -2 Sv. The slope of the boundary between upper and bottom cell becomes almost horizontal with an even shallower depth of ~ 2500 m. The upper circulation cell of the last cycle (Fig. 2d) shows almost no change in shape and magnitude compared to the previous spinup run. The slope and depth of the boundary between upper and bottom cell remains almost constant. These large-scale quantities seem to widely converge within the four spinup cycles. Only the magnitude of the bottom cell further increase slightly to a value of ~ -3 Sv.
Fig. 2e presents the time evolution of the annual maximum AMOC index for all four spinup cycles at 26°N (light gray) and 45°N (dark gray) to distinguish between variabilities that have either a subpolar or a subtropical origin. The AMOC time evolution of the first spinup cycle reveals for the maximum AMOC index at 26°N a decreasing trend in the first third of the simulation period from 1958-1975. In this period the maximum AMOC at 26°N dropped by a value of ~ 3 Sv. After this period the decrease in the AMOC at 26°N is moderate. The maximum AMOC index at 45°N features a more stable behavior with a slight decreasing trend over the entire simulation period of the first spinup cycle. The AMOC indices at 26°N and 45°N of the following spinup cycles do not show such pronounced trends in the time evolution of the AMOC index. The variability in the AMOC strength indicates a common evolution in time for the subsequent spinup cycles. The mean maximum AMOC index at 26°N and 45°N, as indicated by triangles in Fig. 2e, decreases from the first to the last spinup cycle by ~ 1.4 Sv and ~ 1.3 Sv , respectively. The mean and standard deviation of the maximum AMOC index of the last spinup cycle are 9.36 Sv and 0.59 Sv at 26°N and 9.33 Sv and 0.83 Sv at 45°N. The following results of the paper are based on the last spinup cycle.

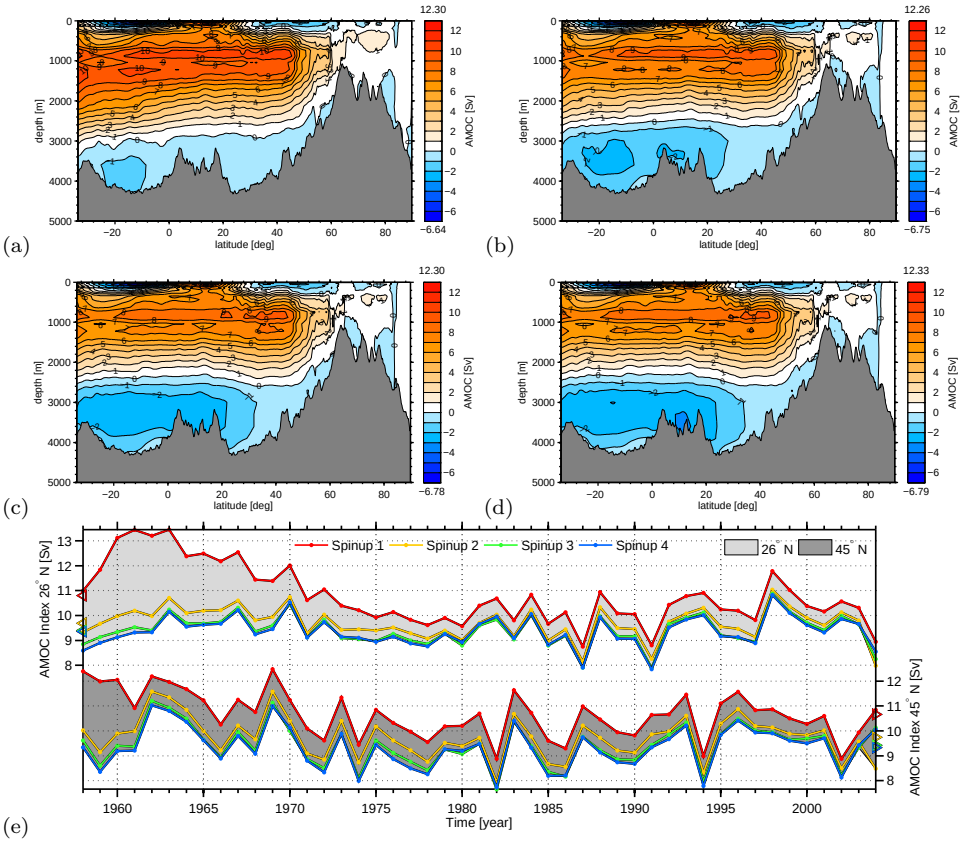

Fig. 2 Mean Atlantic Meridional Overturning Circulation (AMOC) of the first (a), second (b), third (c) and fourth (d) spinup cycle. The simulation period of each spinup cycle goes from 1958-2004. Panel (e) shows the time evolution of the annual maximum AMOC index at 26°N (light gray) and 45°N (dark gray) for all four spinup runs. Triangles mark the values of the mean maximum AMOC index.

3 Evaluation of Sea Ice Model

Sea ice has global effects on the deep water formation and thus the AMOC. Therefore, it is crucial that the sea ice model reproduces realistic sea ice distributions in the polar regions.

Fig. 3 shows the mean Arctic sea ice concentration of the model (Fig. 3 (a),(b)) and observational fields (Fig. 3 (c),(d)), derived from Cavalieri et al (1996, updated 2007) and Meier et al (2006, updated 2007) in March (left column) and September (right column) averaged over the period from 1979-2004. The Arctic winter sea ice cover in March (Fig. 3a) reveals a large coverage over the entire central Arctic region. The March mean sea ice extent (the area where the sea ice concentration was $> 15\%$) reached a value of $14.86 \cdot 10^{12}$ m^2, which is in the order of observational mean sea ice extent values of $15.69 \cdot 10^{12}$ m^2

(Fetterer et al, 2002, updated 2009). The 15% boundary of the winter sea ice concentration extends into the Barents Sea until 75°N and along the east coast of Greenland and the Labrador peninsula until 53°N. The modelled and observational mean sea ice concentration fields in March are in good agreement. The pronounced retreat in the summer Arctic sea ice coverage is clearly seen (Fig. 3b)in the model as well as in the observations. During boreal summer, the Arctic sea ice extent is reduced by around 40% and retreats to a value of $8.91 \cdot 10^{12}$ m^2. The observed Arctic September sea ice extent features a smaller value of $6.91 \cdot 10^{12}$ m^2 (Fetterer et al, 2002, updated 2009). Our model results indicate a slight overestimation of the Arctic summer sea ice extent compared the observations. The modelled results for the summer Arctic sea ice concentration show a relatively high values in the region of the Baffin Bay, that is not identifiable in the observational data showed in Fig. 3d.

Fig. 4 shows the mean Southern Ocean sea ice concentration of the model (Fig. 4 (a),(b)) and observational field (Fig. 4 (c),(d)), derived from Cavalieri et al (1996, updated 2007) and Meier et al (2006, updated 2007) in March (left column) and September (right column) averaged over the period from 1979-2004. The Southern Ocean sea ice concentration in March (Fig. 4a) reveals a region of maximum sea ice concentration of 80% in the Weddell Sea that extends northwards at the east coast of the Antarctic peninsula and gradually decreases, as well as a region of sea ice with concentrations up to $\sim 50\%$ that extends along the western Antarctic coast from the Amundsen Sea to the Ross Sea and Victoria Land coast. The 15% boundary of the Southern Ocean austral summer sea ice concentration barely extends above 70°S. Only in the Weddell Sea it extends as far as ~ 66°S. The minimum sea ice extent in March reached a value of $2.85 \cdot 10^{12}$ m^2, which underestimates the observed March sea ice extent of $4.36 \cdot 10^{12}$ m^2 (Fetterer et al, 2002, updated 2009) by a factor of 1.4. The Southern Ocean mean sea ice concentration in March, reproduced with our model setup, agrees reasonably with the observational results shown in Fig. 4c. The March sea ice extent in the Amundsen Sea and Ross Sea in our model is underestimated compared to the observational data derived from Cavalieri et al (1996, updated 2007) and Meier et al (2006, updated 2007). Furthermore, the observational data does not show an increased sea ice concentration around the Victoria Land coast in contrast to our model results. In austral winter (September), entire Southern Ocean is enclosed by a compact sea ice cover. The sea ice extends until 65°S and encloses an area of $20.16 \cdot 10^{12}$ m^2, which is in the vicinity of the observed value of $18.7 \cdot 10^{12}$ m^2. Comparing to the observational results shown in Fig. 4d, the area with a sea ice concentration $> 90\%$ in our model extends more northward, but the 15% boundary of the sea ice concentration is in a good agreement with observations.

Fig. 5 (a), (b) shows the time evolution of the September Arctic and Southern Ocean sea ice extent of the model (black) and observational (red) data, derived from Fetterer et al (2002, updated 2009). The time evolution of the modelled September Arctic (Fig. 5a) and Southern Ocean (Fig. 5b) sea ice extent for the period 1979-2004 features mean values of $8.25 \cdot 10^{12}$ m^2 and $19.8 \cdot 10^{12}$ m^2,

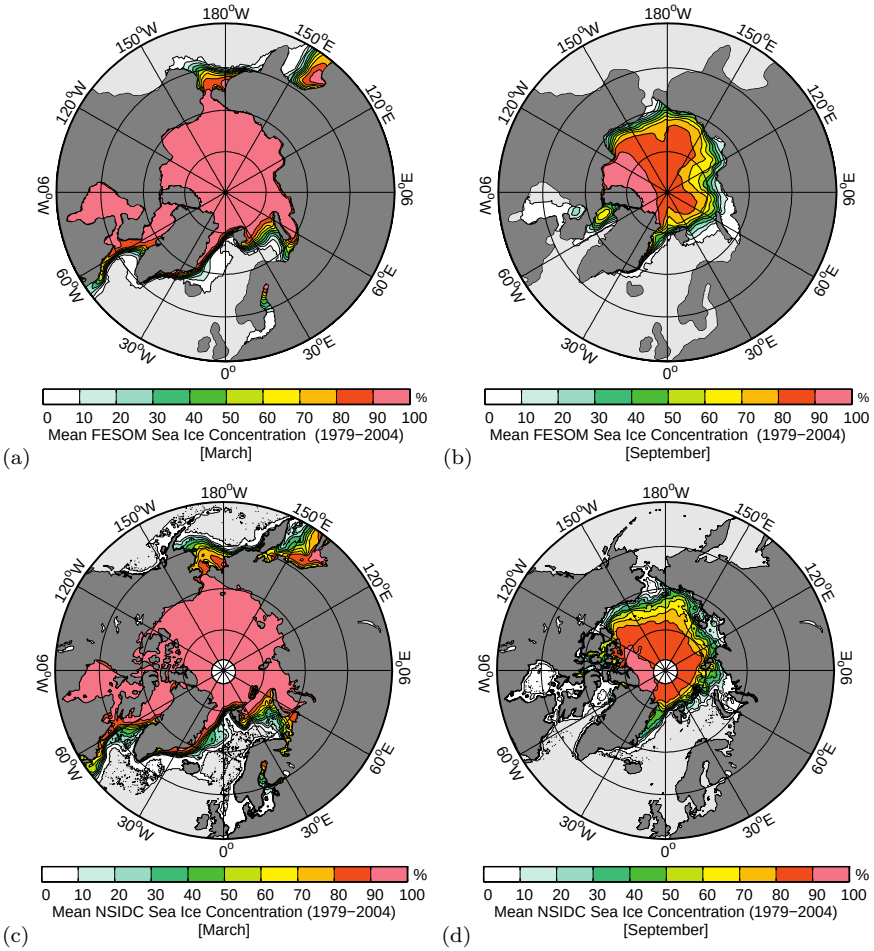

Fig. 3 Simulated (a), (b) and observed (c), (d) mean Arctic sea ice concentration in March (left column) and September (right column). Ice-free areas are marked light gray. The observed fields have been derived from Cavalieri et al (1996, updated 2007) and Meier et al (2006, updated 2007).

respectively. These values are in the order of the observed mean September Arctic and Southern Ocean sea ice extent of $6.9 \cdot 10^{12}$ m^2 and $18.7 \cdot 10^{12}$ m^2, respectively. The Arctic as well as the Southern Ocean sea ice extent time series show a pronounced interannual to decadal variability. The variability of the Arctic sea ice extent for the period of 1979-2004 fits the variability of the observational data with a correlation of 0.7 (99.99% significance level). The time series of modelled and observed Arctic sea ice extent have a standard deviation of $0.45 \cdot 10^{12}$ m^2 and $0.59 \cdot 10^{12}$ m^2, respectively. The Arctic September sea ice extent reveals a slight decreasing trend over the entire simulation period of $-7\,590$ km^2/yr. This trend is even stronger for the second half of the

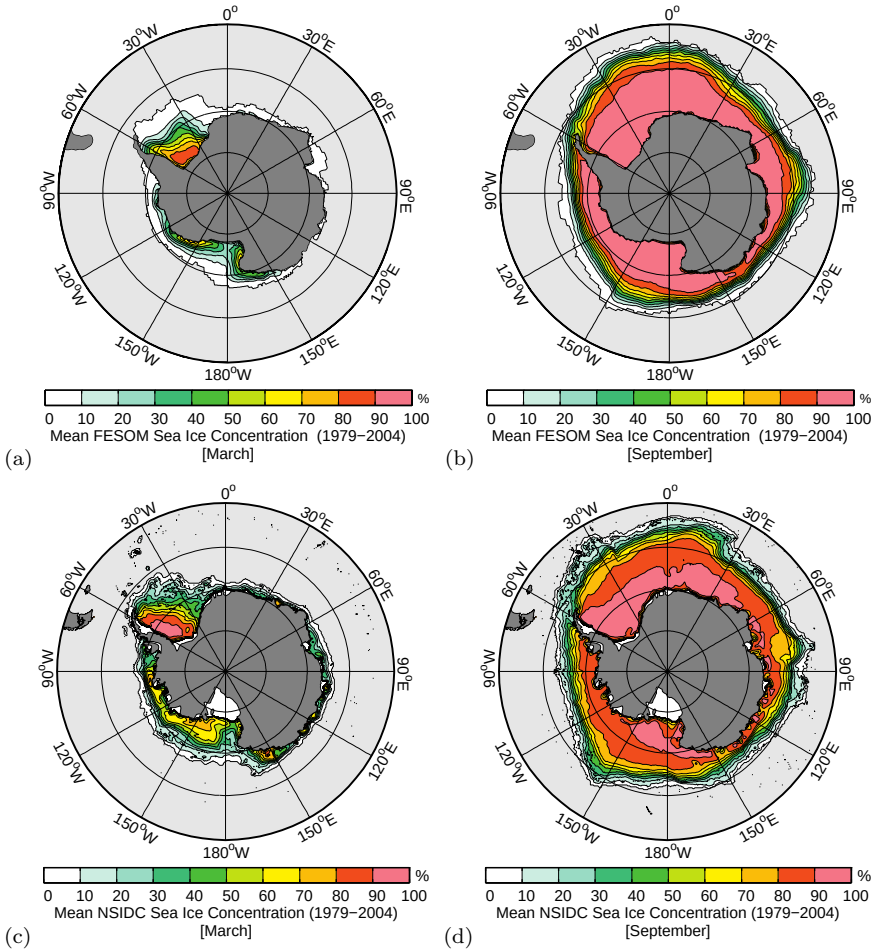

Fig. 4 Simulated (a), (b) and observed (c), (d) mean Antarctic sea ice concentration in March (left column) and September (right column). Ice-free areas are marked by light gray. The observed fields have been derived from Cavalieri et al (1996, updated 2007) and Meier et al (2006, updated 2007).

simulation period from 1979-2004, with a value of $-16\,870$ km^2/yr, whereas the observed Arctic sea ice extent (red) in the interval 1979-2004, features a ~ 3 times higher decreasing trend of $-54\,580$ km^2/yr. The variability of the modelled September Southern Ocean sea ice extent is not significantly correlated with the observational data, although the trend to increasing sea ice extent in the model for the interval 1979-2004 with a value of $8\,390$ km^2/yr is in close agreement with the observed value of $6\,390$ km^2/yr. The trends in the time evolution of the Southern Ocean sea ice extent (Fig. 5b) depends also on the period that is considered. The observed Southern Ocean sea ice extend for the interval 1979-2004 is lower ($\sim 0.7 \cdot 10^{12}$ m^2), compared to the modelled

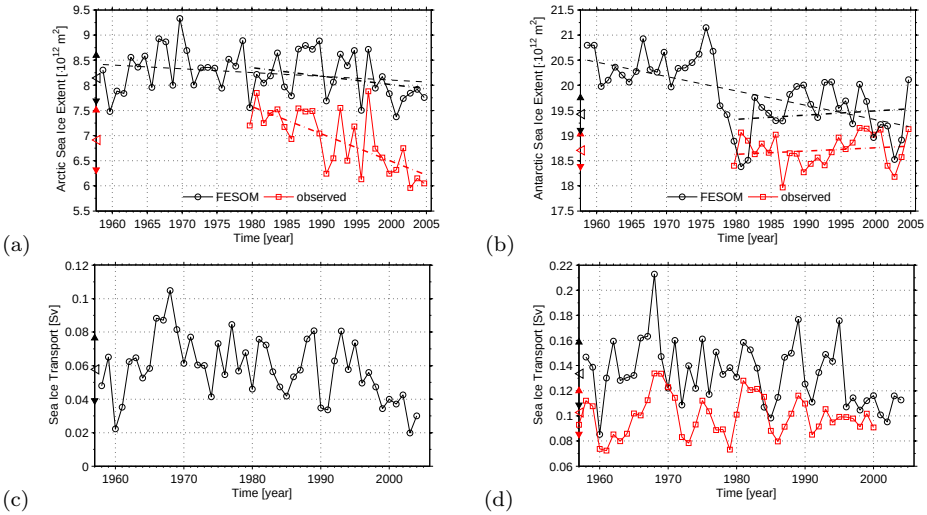

Fig. 5 (a)-(b): Time evolution of the simulated (black) and observed (red) September sea ice extent in the Arctic (a) and Southern Ocean (b). Black and red empty triangles mark the modelled and observed mean sea ice extent, full triangles indicate the upper and lower bound of the standard deviation for the interval 1979-2004. Dashed lines indicate the trend in sea ice extent for the interval 1958-2004 and 1979-2004. The observed sea-ice extent indices has been derived from Fetterer et al (2002, updated 2009).
(c)-(d): Time evolution of the annual sea-ice volume transport through Denmark Strait (c) and Fram Strait (d) (black). The observed (red) annual Fram Strait Sea-Ice volume transport in (d) is derived from Schmith and Hansen (2003).

sea ice extent.

We furthermore calculated the annual sea ice transport over time for a Denmark Strait (Fig. 5c) and Fram Strait (Fig. 5d) cross section. Both time series feature an outstanding high sea ice transport around 1967-1968 followed by smaller events around 1977, 1982, 1988 and 1994. The variability of the modelled Fram Strait sea ice transport matches the observed time series of Schmith and Hansen (2003) with a correlation of 0.51 (99.95% significance level) (Fig. 5d). Fram Strait sea ice transport features a mean and standard deviation of 0.13 Sv and 0.025 Sv for the modelled time series, and 0.10 Sv and 0.017 Sv for the observational derived sea ice transport. Furthermore, the model reveals a constant high sea ice transport between 1970 and 1980. The mean sea ice transport through the Fram Strait for the interval of 1990-1995, with 0.15 Sv, overestimates the upper boundary value of Kwok and Rothrock (1999) with 0.106 Sv by a factor of 1.4.

4 Evaluation of the Ocean Model

4.1 Comparison of Model and OWS data

To further validate our model setup and results, we compared the model data with data from ocean weather ships (OWS) (Lazier, 1980; Levitus et al, 1994). OWS-data provide temperature and salinity profiles between 1950s and 1990s at different positions in the North Atlantic. We compare monthly averaged temperature and salinity time series for different depth layers: 0 m − 100 m, 125 m − 520 m, 620 m − 1640 m and 1880 m − 3600 m (6300 m) at the position of OWS-Bravo (OWS-B, 50.98°W, 56.49°N) and Charly (OWS-C, 35.5°W, 52.75°N) (Fig. 13). We chose these two positions because they allow us to compare the model results of an area with the highest resolution (OWS-B) and an area with coarse resolution (OWS-C), to long term observational data. Although the temperature and salinity of the most upper surface layer (0 m) is mostly prescribed by the surface forcing, it should be mentioned that we averaged here for the surface depth layers over the upper 100 m of the ocean to visualize the model performance beyond the prescribed ocean surface.
The monthly temperature evolution of the OWS-B (orange) and model (green) data shown in Fig. 6a reveal a good agreement for the seasonal cycle in the surface layers for the interval of 1964-1974. The correlation between the monthly and 3-year-running-mean filtered (thick lines) modelled and observational surface data is 0.87 and 0.83 (99.99% significance level), respectively. The monthly data of the intermediate layers of 125 m − 520 m reveal a correlation of 0.31 (99.95% significance level) between the model and the OWS-B data. The 3 year-running-mean filtered data feature in this depth range a correlation negative of −0.46 (99.99% significance level). The OWS-B data of this layer have a maximum in temperature around 1967 with a gradual decrease afterwards. The maximum of the modelled temperature data in this depth layer is around 1971. The 620 m − 1640 m depth layer features for the monthly and 3-year-running mean filtered modelled and observational data a correlation of 0.68 and 0.83 (99.999% significance level), respectively. The modelled and observational data in this depth layer reveals a gradual increase until a temperature maximum around 1971 followed by a subsequent decrease. The observational temperature data of the very deep layers of 1880 m − 3600 m show a higher variability of ~ 1 °C (Fig. 6) compared to the modelled data. The variability in the deep layers of the model is much lower, which is caused to some extent by a much higher number of time steps that is used to calculate the monthly means in the model compared to the observational data. Furthermore, indicate the observed temperature data of the very deep layers an increasing temperature of 0.5 °C over the time period 1964-1974. The modelled temperature time series of the 1880 m − 3600 m depth layers features only a temperature increase of 0.1 °C.
The modelled and observed surface temperature time series at the position of OWS-B has a standard deviation of 1.48 °C and 1.41 °C, respectively. The temperature time evolution of the deeper layers features standard deviations

of the modelled and observed data of 0.19 °C and 0.25 °C in the 125 m − 520 m depth layer, 0.17 °C and 0.16 °C in the 620 m − 1640 m depth layer as well as 0.04 °C and 0.28 °C in the 1880 m − 3600 m depth layer, respectively.
Fig. 6b shows the salinity evolution of the OWS-B (red) and model (blue) data, where the surface layers show a minimum ($\sim$ 34.3 psu) and the intermediate layers (620 m − 1640 m) shows a maximum ($\sim$ 34.9 psu) in the early 1970s. This salinity minimum is well known as a fingerprint of the GSA event that occupied the Labrador Sea around 1970 (see also section 4.4) (Dickson et al, 1988; Haak et al, 2003). The correlation between the monthly and 3-year-running-mean filtered modelled and observed surface salinity data is 0.87 and 0.96 (99.99% significance level), respectively. The model and observed OWS-B salinity time evolution of the intermediate layers 125 m − 520 m reveals also a minimum in the early 1970s. The salinity minimum in the modelled data is therefore much less pronounced. The modelled and observed time series of the monthly and 3-year-running-mean filtered data, reach a correlation of 0.43 and 0.54 (99.99% significance level). The salinity data in the intermediate layers of 620 m − 1640 m feature for the modelled as well as for the observed data a salinity maximum in the early 1970s with a maxima of around 34.9 psu. The correlation in this layer is further decreasing, but still reaches a value of 0.34 (99.98% significance level) and 0.21 (97.54% significance level) for the monthly and 3-year-running-mean filtered data, respectively. The very deep ocean layers of 1880 m − 3600 m reveal in the salinity an offset of $\sim$ 0.04 psu between the OWS-B and model data, but the underlying trend to a slightly increasing salinity is maintained. The variability of the modelled and observed salinity time series of the very deep layers features no significant correlation.
The standard deviations of the modelled and observed salinity time series has surface values of 0.16 psu and 0.17 psu, respectively. The salinity time evolution of the deeper layers features standard deviations of the modelled and observed data of 0.016 psu and 0.048 psu in the 125 m − 520 m depth layer, 0.016 psu and 0.02 psu in the 620 m − 1640 m depth layer as well as 0.005 psu and 0.014 psu in the 1880 m − 6300 m depth layer, respectively.
Fig. 7 shows the modelled and measured monthly and 3-year-running-mean filtered temperature and salinity time evolutions at the position of the OWS-C for the four different depth layers and the interval between 1976 and 1986. The measured (orange) and simulated (green) temperature time series in Fig. 7a features again a good agreement in the seasonal cycle of the surface layer with a correlation of 0.91 (99.99% significance level) between the modeled and observed monthly and 3-year-running-mean filtered data. The simulated temperature time series of the subsequent depth layers differ from OWS-C time series. The simulated intermediate (125 m − 520 m) and deep (1880 m − 6600 m) layers show with respect to the observational data a negative and positive offset. The variability in the deep layers of the model is also much lower compared to the observational data. The correlation between the modelled and observed 3-year-running-mean filtered time series reaches a value of 0.88 (99.99% significance level) for the 125 m − 520 m and 1880 m − 6600 m depth layer. The standard deviations of the modelled and observed temperature time evolution

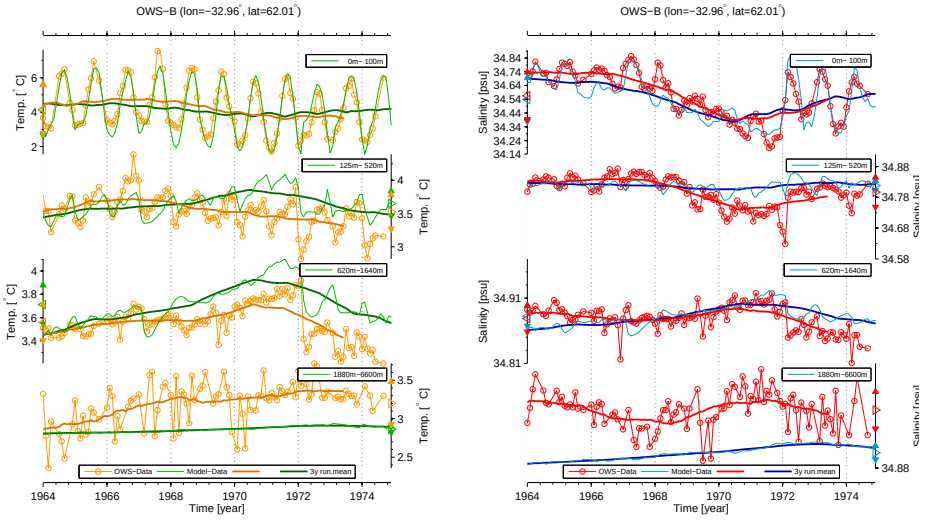

(a) (b)

Fig. 6 Time evolution of the monthly (thin lines) and 3 year-running-mean filtered (thick lines) model and Ocean Weather Station Bravo (OWS-B) temperature (a) and salinity (b) for the period 1958-1974. The OWS temperature and salinity data are indicated by orange and red circles, respectively. The model temperature and salinity data are indicated by green and blue lines, respectively.

at the position of OWS-C, has surface values of 1.66 °C and 1.55 °C, respectively. The temperature time series of the deeper layers features standard deviations of the modelled and observed data of 0.09 °C and 0.33 °C in the 125 m − 520 m depth layer, 0.05 °C and 0.1 °C in the 620 m − 1640 m depth layer as well as 0.04 °C and 0.06 °C in the 1880 m − 6300 m depth layer, respectively.

The salinity time evolutions of the modelled (blue) and measured (red) OWS-C data shown in Fig. 7b reveal a general positive offset between the modelled and measured data through all layers, which decreases with increasing depth. The surface and intermediate layers (125 m−520 m) have an offset of ~ 0.3 psu and ~ 0.1 psu, respectively. The correlation between the modelled and observed monthly averaged and 3-year-running-mean filtered OWS-C salinity time series reveals significant values of 0.82 and 0.94 in the surface layers, 0.68 and 0.95 in the 125 m − 520 m depth layer, 0.42 and 0.82 in the 620 m − 1640 m depth layer as well as 0.27 and 0.67 in the 1880 m − 6300 m depth layer, respectively. The standard deviations of the modelled and observed salinity time evolution, at the position of OWS-C, has surface values of 0.091 psu and 0.107 psu , respectively. The salinity time evolution of the deeper layers reveals standard deviations of the modelled and observed data of 0.035 psu and 0.036 psu in the 125 m − 520 m depth layer, 0.006 psu and 0.017 psu in the 620 m − 1640 m

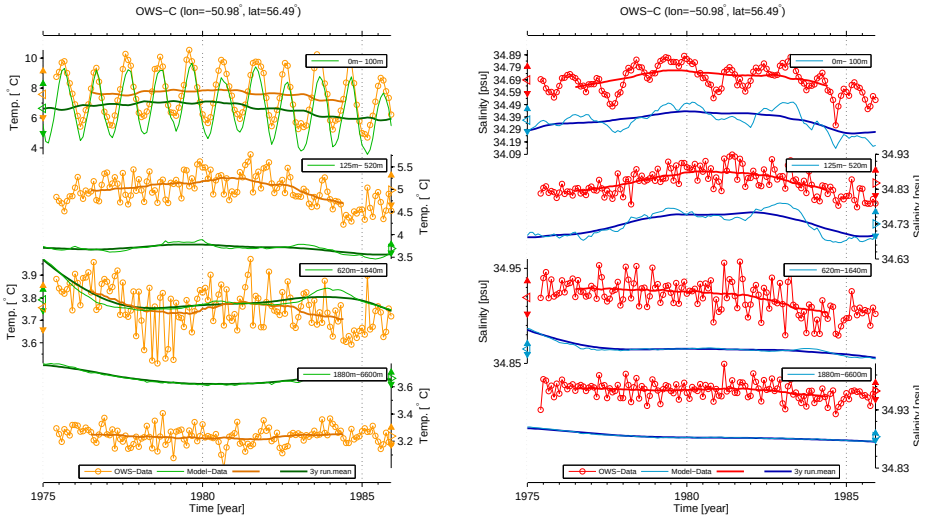

(a) (b)

Fig. 7 Time evolution of the monthly (thin lines) and 3 year-running-mean filtered (thick lines) model and Ocean Weather Station Charly (OWS-C) temperature (a) and salinity (b) for the period 1958-1974. The OWS temperature and salinity data are indicated by orange and red dots, respectively. The model temperature and salinity data are indicated by green and blue lines, respectively.

depth layer as well as 0.006 psu and 0.014 psu in the 1880 m − 6300 m depth layer, respectively.

4.2 Nordic Seas Overflow

The Nordic Sea overflow water is one of the main sources of the deep water in the North Atlantic. To observe the overflow quantities over time, we calculated for cross sections through the Denmark Strait (Fig. 8a) and the Iceland-Scotland Ridge (Fig. 8b) the 3-year-running-mean filtered mean temperature (Fig. 9a, 11a) and mean salinity (Fig. 9b, 11b), for different depth layers of 0 m − 100 m, 125 m − 350 m and 430 m − 880 m. The filtered temperature and salinity in the surface layer (0 m − 100 m) of the Denmark Strait cross section reveals a distinct decadal variability. The filtered time evolution shows a pronounced minimum in the temperature and salinity around 1967 (Fig. 9). The analysis of horizontal salinity distribution (not shown) revealed that this minimum corresponds to a negative salinity anomaly that passes the Denmark Strait and travels within the subpolar gyre. Similar, but weaker negative salinity anomalies pass the Denmark Strait around 1976, 1987 and 1995 (Fig. 9b). The negative salinity anomaly events corresponds with a negative temperature anomaly on the surface (Fig. 9a). These four anomaly events coincide with a high sea ice transport from Arctic shown in Fig. 5c and 5d.

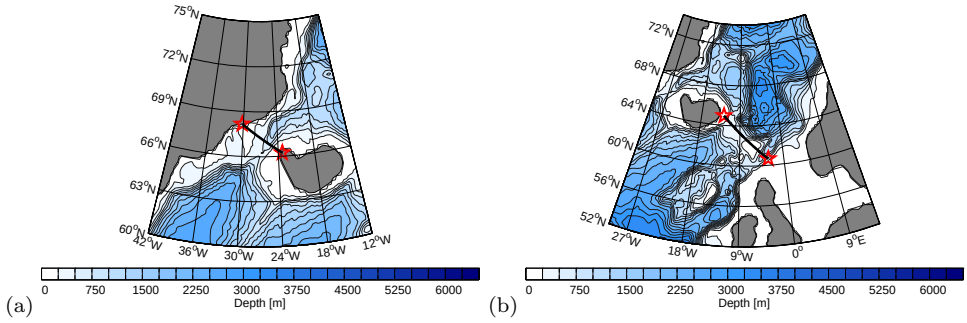

Fig. 8 Position of the Denmark Strait (a) and Iceland-Scotland Ridge (b) cross-section.

The temperature evolution of the filtered time series in the intermediate layers (125 m − 350 m) shows a strong decadal variability with increasing amplitude until the late 1980s. The minima events in the temperature of the intermediate layers corresponds with the one on the surface (Fig. 9a). The salinity evolution in the intermediate layers reveals a slight freshening trend almost over the entire simulation period from 1958 until 1995. The negative surface salinity anomalies of 1967, 1987 and 1995 are also identifiable in the intermediate layers except the surface salinity anomaly of 1975 (Fig. 9b). In 1995 the filtered time evolution of the intermediate layers of temperature and salinity reached its lowest level with a value of −0.45 °C and 33.84 psu, respectively. After that, the temperature and salinity in the intermediate layers increases again until the end of the simulation period.

The freshening trend in the salinity of the intermediate layers is continued in the deep layers (430 − 880 m) (Fig. 9b). While the salinity evolution in the deep layers shows again a slight minima around 1967 and 1995 that originate from the surface anomaly, it features also a salinity minima around 1982. This salinity minima is neither identifiable in the surface or intermediate layers. The time evolution of the deep-layer temperature shows a pronounced decadal variability with an amplitude of 0.5 °C and an underlying slight cooling trend over the entire simulation period. All negative temperature anomalies from the surface are also detected in the deep layers. Fig. 10 illustrates the propagation of a modelled negative surface salinity anomaly (SSA) that traveled within the pathway of the subpolar gyre and passed the Denmark Strait between 1967 and 1968 (see Fig. 9b). The negative SSA propagates then within the East and West Greenland current and reaches the Labrador Sea around two years after it passed the Denmark Strait. Around 1970 the negative SSA reaches the Labrador Current and spills from there in the central North Atlantic Ocean. From here it crosses the Atlantic Ocean from west to east and reaches the Iceland-Scotland Ridge around 1972-1973.

Fig. 11 shows the time evolution of the 3-year-running-mean filtered temperature and salinity, averaged on a cross section through the Iceland-Scotland Ridge for the layers: 0 m − 100 m, 125 m − 350 m and 430 m − 620 m. The

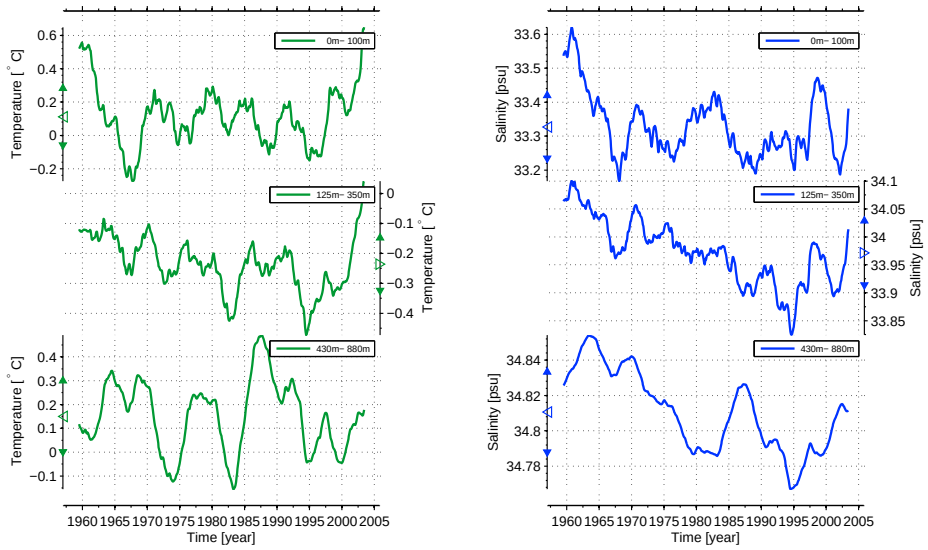

(a) (b)

Fig. 9 Time evolution of the 3-year-running-mean filtered Temperature (a) and Salinity (b) averaged on the cross section through the Denmark Strait for three different depth layers: 0 m − 100 m (upper), 125 m − 350 m (middle) and 430 m − 880 m (lower). The mean temperature and salinity values are marked by empty triangles, filled triangles indicate the upper and lower bound of the standard deviation.

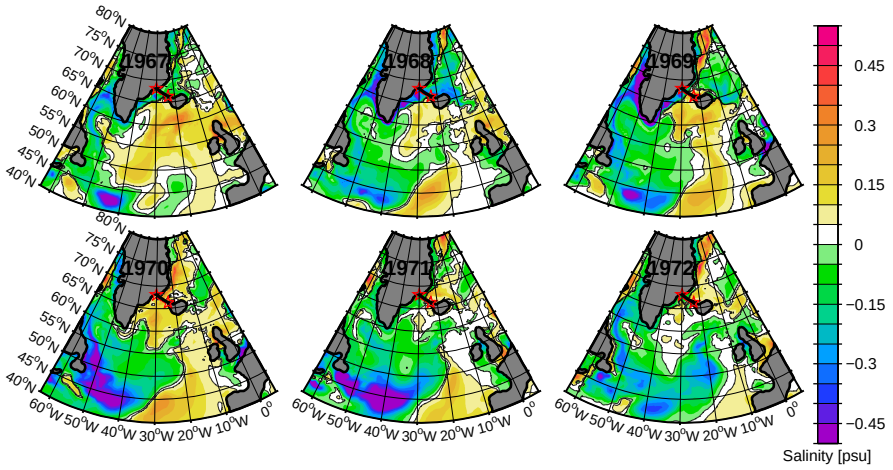

Fig. 10 Horizontal winter (DJF) salinity anomaly distribution in the North Atlantic Ocean for the years 1967, 1968, 1969, 1970, 1971 and 1972 averaged for the depth layers 0 m−100 m. Red stars indicate the position of the Denmark Strait cross-section.

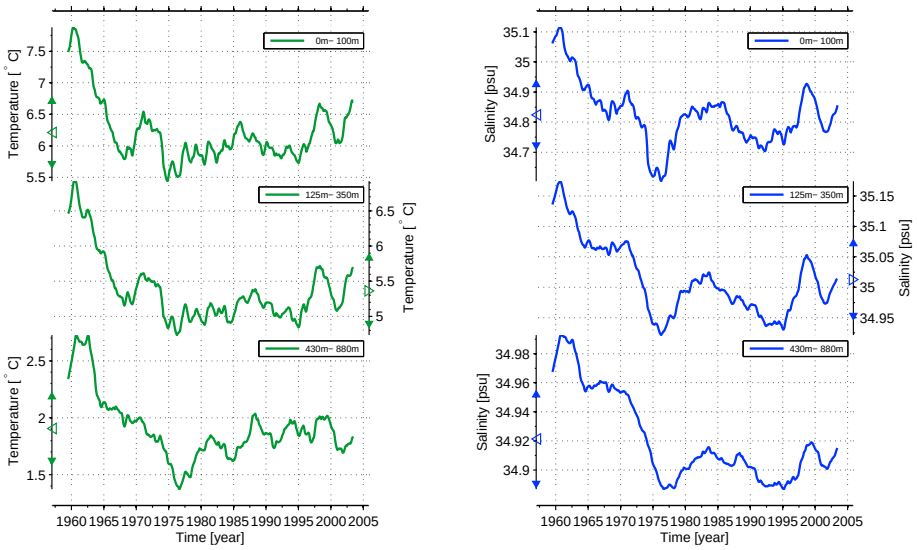

(a) (b)

Fig. 11 Time evolution of the 3-year-running-mean filtered Temperature (a) and Salinity (b) averaged on the cross section through the Iceland-Scotland Ridge for three different depth layers: 0 m − 100 m (upper), 125 m − 350 m (middle) and 430 m − 880 m (lower). The mean temperature and salinity values are marked by empty triangles, filled triangles indicate the upper and lower bound of the standard deviation.

temperature in all layers features a pronounced cooling trend of almost 2.3 °C until 1976 with a minimum value in the surface and deep layers of 5.5 °C and 1.7 °C. After that, the temperature shows a slight warming trend of around 0.7 °C until the end of the simulation period. The temperature evolution in all three layers runs synchronously. From 1958 until 1976, the salinity time series in the Iceland-Scotland Ridge reveals a strong freshening trend of ~ 0.5 psu in the surface layers and ~ 0.22 psu and 0.15 psu in the intermediate and deep layers, respectively. The minimum value is reached around 1976 with a value of ~ 34.6 psu on the surface. After 1976, the salinity increases again until the middle of the 1980s, followed by a renewed freshening that reaches its lowest level around 1995. Analysis of horizontal salinity distribution in the intermediate layers revealed that both salinity minima from 1976 and 1995 originate from a negative salinity anomaly that passed the Denmark Strait around 1967 and 1987, traveled within the subpolar gyre and recirculated over the Iceland-Scotland Ridge back to the Greenland Sea (not shown).

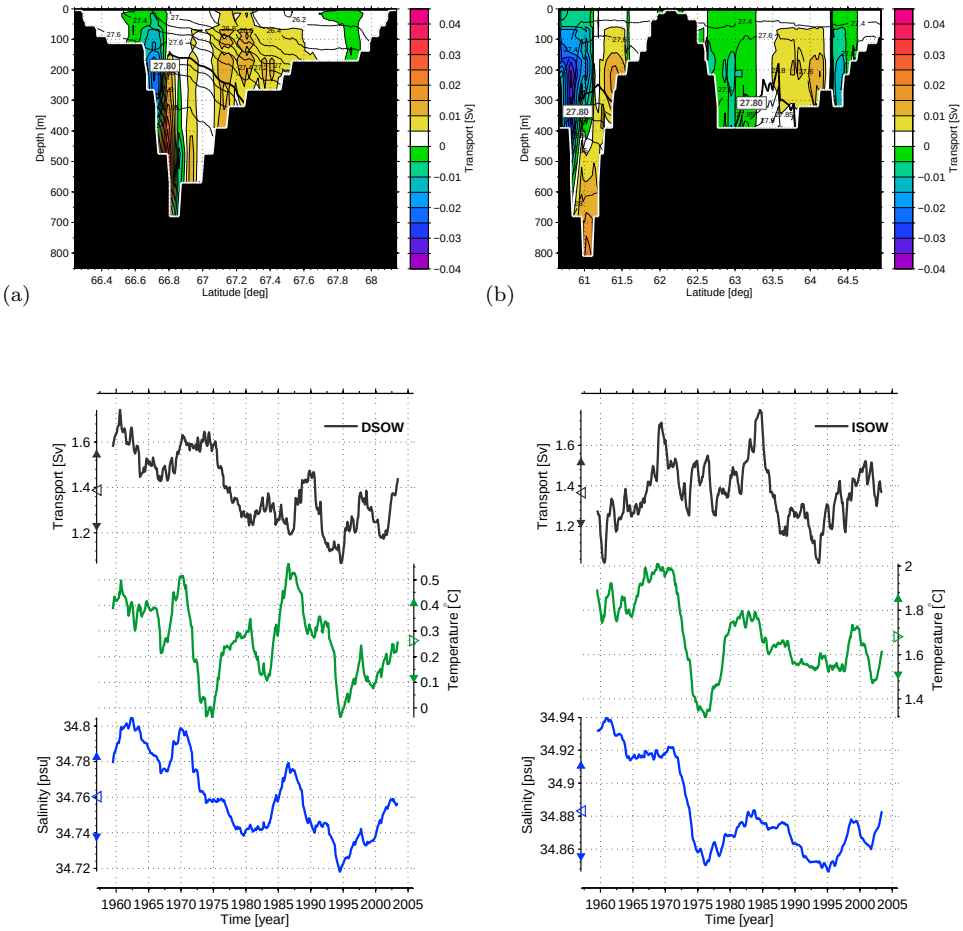

Fig. 12 (a)-(b): Vertical sections of normal directed volume transport (color code) through Denmark Strait (a) and Iceland-Scotland Ridge (b) cross-sections (see Fig. 8). White to reddish colors mean southward directed transport, while green to purple colors mean northward directed transport. Superimposed are the contour lines of the potential density, where the $\sigma_\theta = 27.80\,\mathrm{kg\,m^{-3}}$ isopycnal is highlighted by a thick contour line.
(c)-(d): Time evolution of the 3 year-running-mean filtered normal volume transport (black), temperature (green) and salinity (blue) of the Denmark Strait Overflow Water (DSOW) (c) and Iceland Scotland Overflow Water (ISOW) (d). Empty triangles denote the time averaged values of the corresponding quantity, filled triangles indicate the upper and lower bound of the standard deviation. The overflow waters are defined by potential density $\sigma_\theta > 27.8\,\mathrm{kg\,m^{-3}}$ and southward directed transport.

4.3 DSOW and ISOW

The densest water masses that spills via the Denmark Strait and the Iceland-Scotland Ridge into the abyssal basin of the North Atlantic are the Denmark Strait Overflow Water (DSOW) and the Iceland Scotland Overflow Water (ISOW). The presence of both water masses can be found throughout large parts of the Atlantic basin below a depth of 1000 m (Curry et al, 2003). DSOW and ISOW are part of the bulk water masses that form the southward-flowing lower limb of the AMOC. In this study we define the overflow water masses of DSOW and ISOW by potential densities $\sigma_\theta > 28.80\,\mathrm{kg\,m^{-3}}$ (Dickson and Brown, 1994; Girton and Sanford, 2001) and southward directed flow that pass the Denmark Strait and Iceland-Scotland Ridge cross-section of Fig. 8.
The vertical cross-section of the normal directed volume transport through the Denmark Strait and the Iceland-Scotland Ridge cross-section averaged for the time interval 1958-2004 is presented in Fig. 12(a) and 12(b), respectively. The $\sigma_\theta = 28.80\,\mathrm{kg\,m^{-3}}$ isopycnal is highlighted by a thick contour line and southward directed flow is indicate by white to reddish colors. The vertical mean cross-section of the normal directed Denmark Strait volume transport (Fig. 12a) indicates a major southward directed maximum transport of 0.04 Sv in the density branch of the DSOW in a narrow band at the southern flank of the Denmark Strait. Whereas the normal directed volume transport of the Iceland-Scotland Ridge cross-section (Fig. 12b) reveals a pronounced southward directed maximum transport of 0.025 Sv in the density branch of the ISOW in the Faroe-Shetland Channel.
The time evolution of the 3 year-running-mean filtered modelled DSOW and ISOW, volume transport, temperature and salinity through the Denmark Strait and Iceland-Scotland Ridge cross-section is displayed in Fig. 12(c) and Fig. 12(d), respectively. The time evolution of the DSOW volume transport (black line) reveals a mean value of ~ 1.4 Sv and a significant decreasing trend for the interval 1958-1995 followed by an increasing trend until the end of the simulation period. Besides the underlying trends, the DSOW volume transport features maxima around 1960, 1972, 1983, 1990 and 1997, respectively. The filtered DSOW temperature (green line) and salinity (blue line) time evolution reveals a mean value of 0.24 °C and 34.76 psu, respectively. The time series of the DSOW salinity reveals a general freshening trend for the period 1958-1995. Both time series feature several maxima, that match the aforementioned time evolution of the temperature and salinity of the $125\,\mathrm{m} - 350\,\mathrm{m}$ and $430\,\mathrm{m} - 880\,\mathrm{m}$ depth layers in Fig. 9.
The 3 year-running-mean filtered time series of ISOW volume transport shows a mean value of ~ 1.4 Sv, where no distinct trend is visible. There are two outstanding maxima in the ISOW volume transport at the end of the 1960s and in the middle of the 1980s. The time series of the 3 year-running-mean filtered ISOW temperature and salinity show a trend to colder and fresher overflow waters over the entire simulation period. Both time series are characterize by a strong drop in temperature and salinity in the early 1970s that reach its minimum values ~ 1976 followed by a temperature and salinity increase until

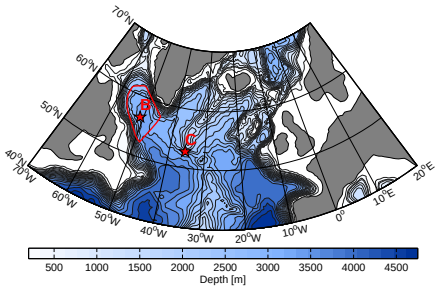

Fig. 13 Position of the index selection area (red contour) in the Labrador Sea that was used to compute the temperature and salinity indices of Fig. 19. The index was computed as the mean of all node points that are located within the red contour line. The Position of the Ocean Weather Ships (OWS) Bravo (B) and Charly (C) are marked by red stars.

the early 1980s. This decrease in temperature and salinity is accompanied by a reduction in the ISOW volume transport.

4.4 Great Salinity Anomaly events

To have a closer look at the evolution of the deep ocean temperature and salinity we calculate for an area in the Labrador Sea (Fig. 13, red contour) a detrended and 3-year-running-mean filtered, temperature (Fig. 14a) and salinity (Fig. 14b) index over depth and time. The filtered temperature and salinity index reveals several positive and negative anomalies at the surface and deep ocean layers, that reach into depths of $2000 - 2500$ m. In the early 1960s, the surface layers of both indices to a depth of ~ 100 m are occupied by a positive temperature and salinity anomaly of ~ 0.3 °C and ~ 0.12 psu, respectively. While the lower layers to a depth of ~ 2500 m show a maximum cooling and freshening anomaly of ~ -0.3 °C and ~ -0.02 psu. In the late 1960s to the early 1970s the situation is reversed. Now the surface layers show a cooling and strong freshening event of around ~ -0.2 °C and ~ -0.1 psu, while the lower layers to a depth of ~ 2000 m show a maximum warming and increase in the salinity of ~ 0.4 °C and 0.04 psu. This event shows the typical fingerprint of the Great Salinity Anomaly (GSA) event of 1970, that is described by Dickson et al (1988). At the beginning and at the end of the 1980s there are two similar but weaker warming and increased salinity events of the deeper ocean layers, with a maximum warming and salinification of ~ 0.2 °C and ~ 0.02 psu. These two GSA events are also present in observational data and are further described by Belkin et al (1998) and Belkin (2004). These two events are separated by a strong surface cooling and freshening of ~ -1.3 °C and ~ 0.1 psu in the upper 100 m of the ocean around 1984. The surface freshening event extends thereby over the entire 1980s. In the middle of the 1990s, the temperature and salinity index reveals again a pronounced cooling and freshening anomaly of ~ -0.4 °C and ~ -0.02 psu, respectively. This negative temperature and salinity anomaly reaches from the surface into depths

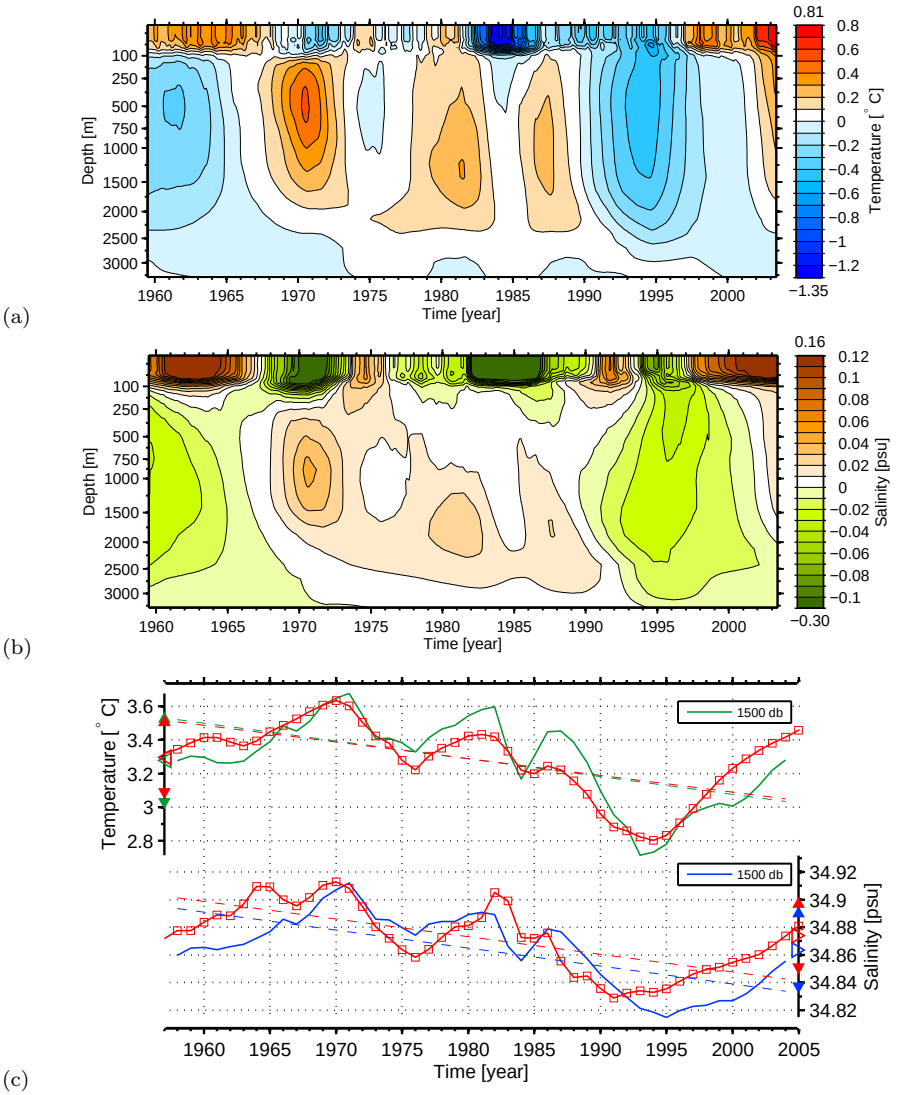

Fig. 14 (a)-(b): Modelled temperature (a) and salinity (b) index over depth and time for the index selection area described in Fig. 13. The data are detrended and smoothed with a 3-year-running-mean filter.
(c): Modelled and observed (red) annual temperature and salinity time series at a pressure level of 1500 dbar in the central Labrador Sea. The observational data are provided by van Aken et al (2011). The mean and the upper and lower bound of the standard deviation of the temperature and salinity time series are marked by empty and filled triangles, respectively. Dashed lines indicate the trend in temperature and salinity trend for the entire simulation period.

of 2500 m. Towards the end of the simulation period, the model indicate a new warming and positive salinity anomaly that reaches from the surface to intermediate depths.
Fig. 14c presents the annual modelled and observational derived (van Aken et al, 2011) temperature and salinity time series at a pressure level of 1500 dbar in the central Labrador Sea between 1958-2004. The modelled (green) and observational derived (red) temperature time evolution reveals a mean value of 3.28 °C and 3.3 °C with a standard deviation of 0.25 °C and 0.21 °C, respectively. The variability of both time series is correlated with a value of 0.8 (99.99% significance level). The time evolution of the modelled and observed temperature features three maxima around 1970/1971, 1982 and 1986/1987 followed by a temperature minimum around 1993 and a subsequent increase in temperature until the end of the simulation period. These findings coincides with the modelled temperature behavior of deeper layers shown in Fig. 14a. The amplitudes of the temperature maxima of 1982 and 1986/1987 are less pronounced in the observational data. Modelled and observed temperature data exhibit over the entire simulation period a trend of -0.011 °C/yr and -0.010 °C/yr, respectively.
The modelled (blue) and observational derived (red) salinity time evolution features a mean value of 34.86 psu and 34.87 psu with a standard deviation of 0.03 psu and 0.02 psu, respectively. The comparison between the modelled and observed salinity data of van Aken et al (2011) shows a correlation of 0.61 (99.999% significance level). The modelled 1500 dbar salinity time series has maxima around 1971, 1982 and 1986/1987, respectively. The maxima in the observed salinity time series are mostly consistent with the modelled maxima, except that the observational derived salinity data feature a further maxima around 1964. The absolute salinity minimum around 1995 in the modelled data is shifted in the observational data towards 1991. Modelled and observed salinity data reveal over the entire simulation period a trend of -0.001 psu/yr.

4.5 Comparison of modelled and observed mixed layer depth

The mixed layer in the ocean is formed by different processes that lead to a mixing and homogenization of the water column. Processes that contribute to the formation of a mixed layer are wind-driven mixing, Ekman pumping and convective mixing of unstable water columns (Griffies et al, 2009). The latter process of convective mixing, forms the downwelling limb of the Meridional Overturning Circulation, which is essential for the formation of dense water masses like the North Atlantic Deep Water (NADW) and Antarctic Bottom Water (AABW). The thickness and location of the mixed layer formed in late winter is thus an important estimator for the strength and position of the deep water formation areas.
Fig. 15 (a) and (b), shows the modelled and observational derived (de Boyer Montegut et al, 2004) climatological March mixed layer depth (MLD). The modelled climatology features in the North Atlantic four regions with a significant

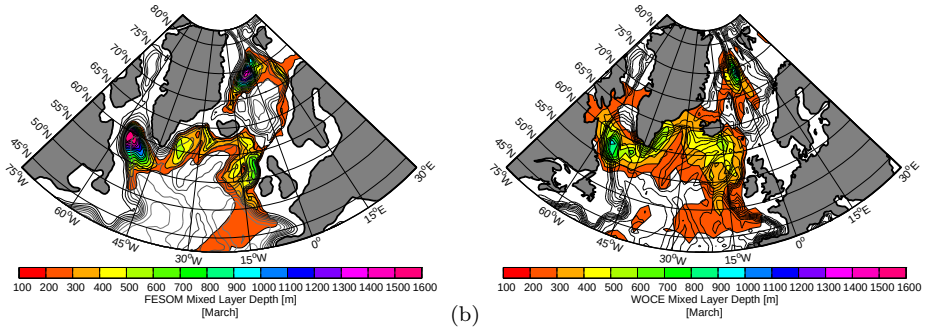

Fig. 15 Modelled (a) and observed (b) climatological maximum mixed layer depth in March. The observational data are derived from de Boyer Montegut et al (2004). Contour lines indicate the bottom topography in steps of 500 m.

MLD that are located in: the Labrador Sea, the Irminger Sea, northwest of the British Isles and the Greenland-Norwegian Sea. The main deep convection areas in the Labrador Sea and Greenland Sea reach a MLD of $\sim$ 1600 m. The MLD in the Irminger Sea and northwest of the British Isles features shallower values of $\sim$ 500 m and $\sim$ 700 m,respectively.
The observational derived climatological MLD of de Boyer Montegut et al (2004) also features two main convection areas in the Labrador Sea and Greenland Sea with a maximum MLD of $\sim$ 900 m and $\sim$ 1000 m, respectively. The observed MLD in the Irminger Sea has a maximum value of $\sim$ 500 m with a center that is shifted towards the coast of Greenland compared to the modelled MLD. The increased MLD in the model, northwest of the British Isles is shifted in the observational derived MLD towards Iceland and reaches there values of $\sim$ 500 m.

4.6 Comparison of modelled and observed WOCE hydrographic sections A1E

The WOCE hydrographic section A1E extents from southern tip of Greenland to the Irish coast (Fig. 16a). The section crosses the Irminger Sea and the Reykjanes Ridge as well as in the Iceland Basin the eastern branch of the subpolar gyre which is associated with the path of North Atlantic Current (NAC) (Bersch, 1995; Bersch et al, 1999). Fig. 16b and c presents the vertical temperature and salinity distributions of the WOCE hydrographic section A1E measured by the RV Meteor cruise in September 1991. The surface layers ($\sim$ 200 m) of this sections are occupied in the eastern branch by warm and saline water masses, which belong to the Subpolar Mode Water (SPMW) that is transported northward. At $\sim$ 30°N, the measured vertical temperature and salinity section features in the upper layers ($\sim$ 300 m) values of $\sim$ 7 °C and $\sim$ 35.1 psu, respectively. These values originate from already cooled and fresh SPMW that flows along the eastern flank of the Reykjanes Ridge (Bersch et al, 1999). The intermediate layers (750 m-2000 m) of the section , contains

Labrador Sea Water (LSW) that spilled eastward along the North Atlantic and can be identified by its salinity minimum that extents over the entire section. The deep layers of the western part of the A1E section are occupied by a less saline DSOW, while the eastern flank of the Reykjanes Ridge is occupied with more saline ISOW (Bersch, 1995; Bersch et al, 1999).
The modelled temperature and salinity A1E hydrographic section in September 1991 are shown in Fig. 16d and e, respectively. Eastward of the Reykjanes Ridge these sections reveal in the surface layers a warm and saline water body. The temperature cross sections of the modelled and measured A1E section show a good agreement, while the modelled salinity cross section indicate in the upper layers a shift of the saline water body towards the Irish coast. Compared to the observed cross section, the maximum of the modelled salinity section is located in a greater depth of ~ 500 m. The surface layers (< 100 m) of the modelled cross-section feature a low salinity body that extends from the Irminger Sea eastward almost along the entire section. The measured section shows mostly a low salinity body that is located in the Irminger Sea. The salinity of the SPMW that flows southward along the the eastern flank of the Reykjanes Ridge is deeper located and less expressed in the modelled cross section. The very deep layers of the modelled cross-section that are associated with the DSOW and ISOW reveal a general lower salinity compared to the observed A1E cross-section.

4.7 Variability in the Atlantic Meridional Overturning Circulation

To visualize the large scale variability of the model, we will use the maximum annual AMOC index at 45°N shown in Fig. 17, which features a strong decadal variability that varies between 7.7 - 11 Sv with a mean value of 9.33 Sv and a standard deviation of 0.83 Sv. The maximum and minimum phase of the AMOC index are indicated by dark and light gray shadings, respectively. There are pronounced maxima in the intensity of the AMOC in the early and late 1960s, around 1984 as well as in the early and late 1990s. Minima in the intensity of the AMOC are in the 1970s until the early 1980s as well as in the late 1980s and around 1994 and 2002.
To further extract the important patterns that coincide with a maximum and minimum AMOC index, we applied a Composite Map Analysis (von Storch and Zwiers, 2003) between the annual maximum AMOC index and different meridional and horizontal quantities. For the calculation of the high (low) composites we used all time slices that are above (below) 75% of the standard deviation of the AMOC index. The time slices for the high (low) composites are marked in Fig. 17 by red (blue) circles.
Fig. 18 (a) and (b) show the high and low composite maps of the annual mean AMOC profile, respectively. The upper circulation cell of the high AMOC composite (Fig. 18a) is ~ 2 Sv stronger comparing to the low AMOC composite (Fig. 18b) and reaches at a latitude of 40° N around 300 m deeper. The magnitude of the counter clockwise wind-driven surface circulation cell

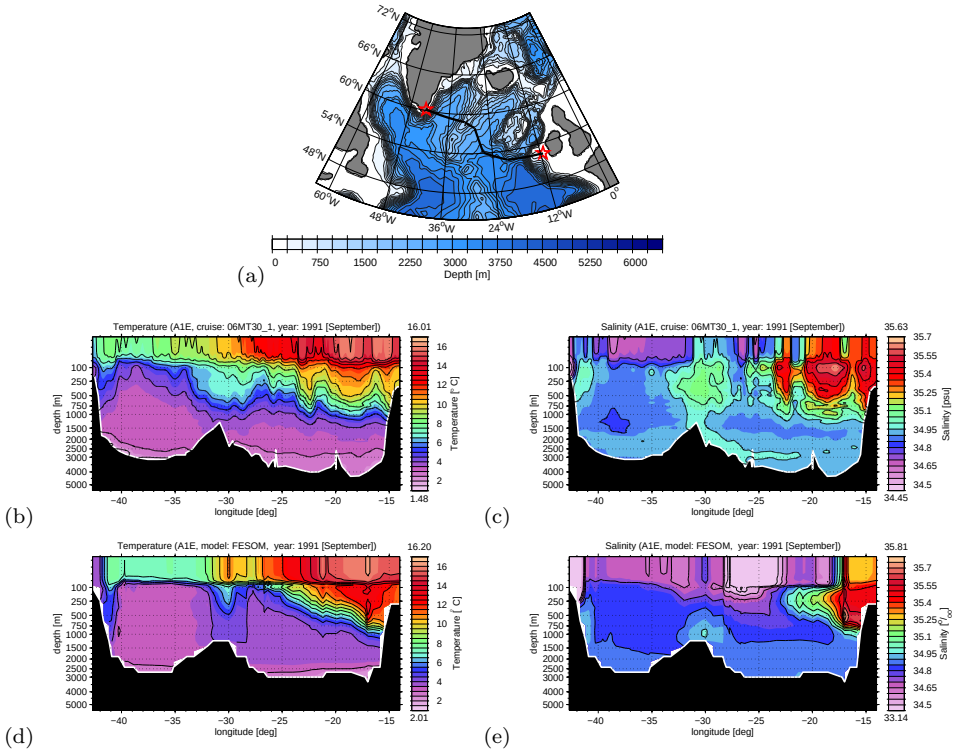

Fig. 16 (a): Position of the Wold Ocean Circulation Experiment (WOCE) hydrographic sections A1E between Greenland and Ireland in the year 1991 (Meincke, 1991). (b)-(c): Observed temperature (b) and salinity (c) WOCE A1E hydrographic section measured in September 1991 (Schlitzer, 2000). (d)-(e): Analogue model temperature (d) and salinity (e) A1E section in September 1991.

at $\sim 48^{\circ}$N is increased by ~ 1 Sv comparing to the low AMOC composite. The magnitude of the bottom circulation cell is the same for the high and low AMOC composites, but the -1 Sv streamline of the bottom circulation cell in the low AMOC composite (Fig. 18b) extents more northward until 52°N.

Fig. 18 (c) and (d) shows the high and low composite maps for the winter (DJF) mean MLD, respectively. The most dominant deep-water formation areas for high AMOC (Fig. 18c) are at the continental slope of eastern Greenland with a MLD of ~ 1000 m and in the Labrador Sea with a MLD of ~ 850 m. The MLD in the remaining two areas in the Irminger Sea and northwest of the British Isles reach only at intermediate depths of ~ 400 m and ~ 550 m, respectively. For low AMOC (Fig. 18d) the MLD at the continental slope of eastern Greenland and in the Labrador Sea decreases to a depth of ~ 700 m and ~ 650 m, respectively. The MLD at the continental slope northwest of the British Isles is decreases as well by ~ 100 m during low AMOC.

Fig. 19 shows the difference composite maps (high-low) for the zonal averaged meridional temperature (Fig. 19a) and salinity (Fig. 19b) profiles in the

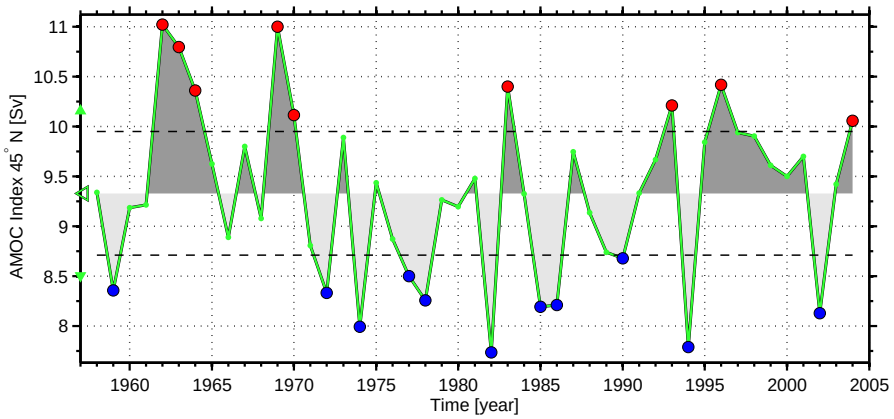

Fig. 17 Annual time evolution of the maximum AMOC at 45°N (solid line). The maximum and minimum phase of the AMOC are marked by dark- and light gray shaded areas, respectively. The 75% limits of above (below) standard deviation are indicated by dashed lines. Time slices when the AMOC index was above (below) 75% of standard deviation are marked by red (blue) circles. An empty triangle marks the value of the time averaged AMOC index, while filled triangles indicate the upper and lower bound of the standard deviation.

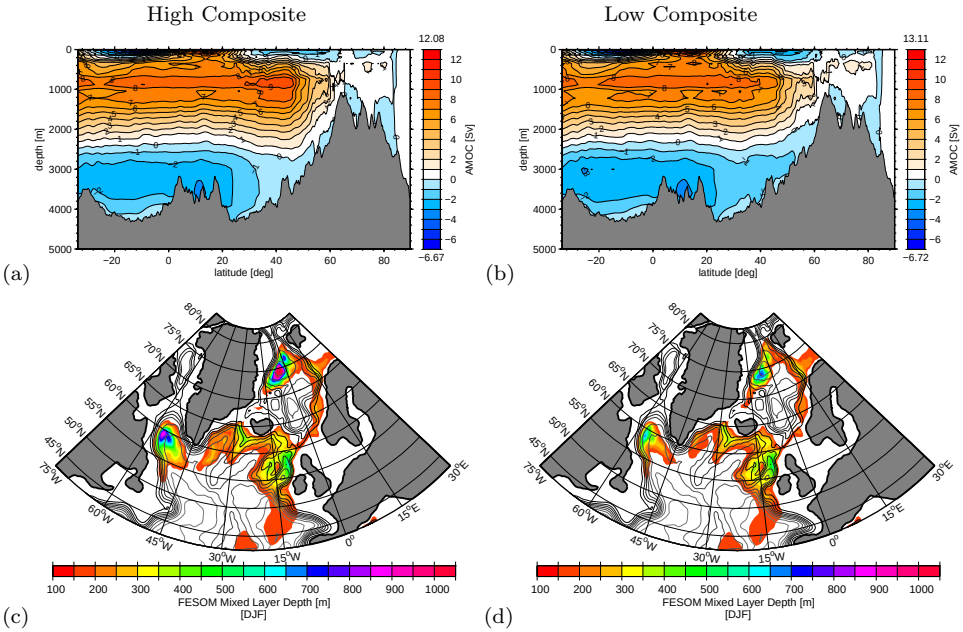

Fig. 18 (a)-(b): High (a) and low (b) composite maps of the annual mean AMOC with the annual maximum AMOC index at 45°N (Fig. 17). The numbers above (below) the colorbar denote the maximum (minimum) values of the wind-driven surface ekman cells.
(c)-(d): High (c) and low (d) composite maps of the winter mean mixed layer depth with annual maximum AMOC index at 45°N (Fig. 17). Contour lines indicate the bottom topography in steps of 500 m.

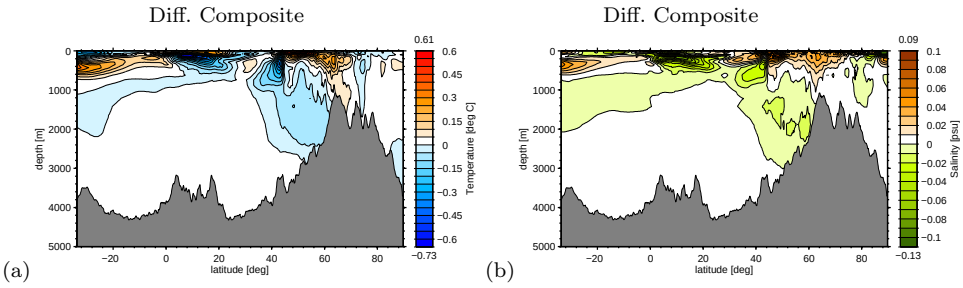

Fig. 19 Difference composite maps (high-low) of the monthly mean meridional Temperature (a) and Salinity (b) profile with annual maximum AMOC index 45°N (Fig. 17).

Atlantic and Arctic Ocean with respect to the annual maximum AMOC index at 45°N above and below 75% of its standard deviation. Both profiles show a strong positive temperature and salinity anomaly between 44°N-64°N with values of $\sim$ 0.3 °C and $\sim$ 0.04 psu, respectively that reach a depth of $\sim$ 1000 m. The subtropical Atlantic and in the middle Atlantic at $\sim$ 35°N at a depth of 400-900 m show a strong negative temperature and salinity anomaly of ~ -0.7 °C and ~ -0.12 psu, respectively. The northern branch between 66°N-78°N indicates a negative temperature anomaly of ~ -0.1 °C.

5 Discussion

In this paper we have described a global FESOM setup designed to resolve the deep water formation areas in the Northern Hemisphere (Labrador Sea, Greenland Sea) as well as in the Southern Hemisphere (Weddell Sea, Ross Sea) with locally refined resolution in a global context. The focus of this study was the evaluation of the model setup for the area of the North Atlantic Ocean.
We show that the maximum AMOC index and the upper circulation cell of the AMOC reaches a quasi-equilibrium state within the first $\sim$ 100 years of simulation. This agrees well with the findings of Sidorenko et al (2011) regarding the model spinup. Our spinup results show in addition that the extent of the AMOC bottom cell is almost converged within our four spinup cycles, whereas the magnitude of the bottom cell still shows a slight upward trend.
The mean value of the maximum AMOC index at 26°N and 45°N of approximately 9.3 Sv underestimates the value reconstructed from observational data at 26°N by Cunningham et al (2007) by a factor of 2, but is still at the lower limit of AMOC values presented in Griffies et al (2009) for different model approaches. The mean value matches the results of other FESOM simulations (see e.g. Sidorenko et al, 2009; Wang et al, 2012b). Nevertheless, the interannual maximum AMOC variability in our model with a standard deviation of 0.59 Sv-0.83 Sv, is comparable with values of the historical AMOC reconstruction of Balmaseda et al (2007). The historical AMOC reconstruction of Balmaseda et al (2007) at 50°N shows an above average AMOC strength in the early 1960s, at the beginning of the 1970s, in the middle of the 1980s and

in the entire 1990s which matches our results regarding the variability of the modelled maximum AMOC index at 45°N. Further, the reconstruction of Balmaseda et al (2007)shows an above average AMOC strength in the middle and late 1970s, which deviates from our findings. However, a principal problem for estimate AMOC from observational data is related to the fact that one has to take into account for both variability and observational uncertainty.
The evaluation of the sea ice model revealed that the sea ice concentration in the Arctic and Southern Ocean resembles well the observational fields from Cavalieri et al (1996, updated 2007). The sea ice shows a more realistic sea ice concentration distribution than the FESOM setup shown by Timmermann et al (2009) under NCEP forcing. The increased summer sea ice concentration in the Baffin Bay was neither found in the observational fields or in the modelled FESOM results of Timmermann et al (2009) but resembles well modelled FESOM sea ice concentrations of Sidorenko et al (2011) and Wang et al (2012b), which used the Coordinated Ocean Ice Reference Experiment version 1 (COREv1) data as forcing. Recent studies of Wang et al (2012a) indicate that the unusual high summer sea ice concentration in Baffin Bay is related to atmospheric COREv2 forcing data. Wang et al (2012a) found that the shortwave radiative forcing in the CORE forcing data of Large and Yeager (2008) is underestimated in the area of the Baffin Bay especially in summer. This leads to reduced sea ice melting and an increased summer sea ice concentration.
The comparison of modelled and observed September Arctic and Southern Ocean sea ice extent time series indicates that the sea-ice model is able to reproduce in the Arctic most of the variability that is shown in the observational data (Fetterer et al, 2002, updated 2009). The model tends overestimate the observed summer sea-ice extent by $\sim 1.4 \cdot 10^{12}$ m^2 but underestimates the decreasing trend in observed sea ice extend. This could also be associated with an underestimation of the radiative forcing in the data of Large and Yeager (2008) which results in an lower summer sea ice melting rate (Wang et al, 2012a). The time series of the September sea ice extent in the Southern Ocean for the period 1979-2004 revealed that the variability between the detrended modelled and observed indices is not significant correlated. Therefore the model is able to match the increasing trend in the Southern Ocean sea ice extent in the second half of the simulation period. The jump in the Southern Ocean sea ice extent in the late 1970s could indicate deficiencies in the reanalysis data of the forcing fields as described by Bromwich et al (2007). They found that there is a significant shift in the quality of the Antarctic reanalysis data prior and after the modern satellite era. The comparison of modelled and observed sea ice transport through the Fram Strait revealed that the model is capable to reproduce the variability, although the model tends to overestimate here the observational data from Schmith and Hansen (2003).
The comparison of model and OWS data (Levitus et al, 1994; Lohmann et al, 2008) shows a reasonably good agreement of the temperature and salinity time series, especially at the higher resoluted position of the OWS-B. Although the surface temperature and salinity in our model are mostly prescribed by the forcing, we are able to reproduce very well the vertical signal of the GSA event

that occupied the Labrador Sea in the early 1970s and was captured by the OWS-B (Dickson et al, 1988; Haak et al, 2003). At the position of the OWS-C, where the resolution is already coarser, the model tends to overestimate the salinity by around 0.1-0.3 psu. The offset in the intermediate and deep layers of the temperature time series and the general offset in the salinity time series is mostly related to a shift in the ocean circulation pattern due to the coarser mesh.

GSA events or negative salinity anomalies are substantial signals in the North Atlantic Ocean which had a far-reaching influence on many aspects of the climate. The model features several negative salinity anomalies that pass the Denmark Strait around 1967, 1976, 1987 and 1995, coinciding with a high sea-ice volume export from the Arctic region. Long term observations of the Denmark Strait salinity of Dickson et al (2002) and Eldevik et al (2009) document similar negative salinity anomalies around 1967, 1978 and 1995. The salinity minimum in the deeper layers (430 m − 880 m) of the Denmark Strait cross-section around 1982, that is not identifiable in upper layers is related to a freshening event of the Denmark Strait Overflow Water (DSOW) which is confirmed by observational data of Dickson et al (2002).

The analysis of the DSOW and ISOW volume transport revealed, for both water masses, a mean transport of approximately 1.4 Sv. Observational estimations of the DSOW transport (Girton and Sanford, 2001; Macrander et al, 2007; Sarafanov et al, 2009) suggest a general stronger overflow in the range of 2.5 − 3.0 Sv. Further, the modelled mean salinity range of the DSOW (34.78 psu) and ISOW (34.89 psu) is too fresh compared to observed estimates, which suggest a DSOW and ISOW salinity in the range of 34.88 − 34.94 psu and 34.98 − 35.03 psu, respectively (Warren and Wunsch, 2007). The model generally tends to underestimate the transport and salinity of the DSOW and ISOW overflows, which is an explanation for the reduced strength and size of the upper AMOC circulation cell in the model as described by different authors (e.g., Döscher and Redler, 1997; Latif et al, 2006; Zhang et al, 2011). Nevertheless, the underlying trends and variabilities in the salinity time series of the DSOW overflow water matches well the observation of Dickson et al (2002) and Eldevik et al (2009), which revealed a freshening trend of the DSOW over the last four decades as well as a salinity minimum in the late 1970s to early 1980s. Further, the modelled time evolution of the DSOW volume transport features a distinct interannual to decadal variability as it mentioned in the first long-term overflow observation at the Denmark Strait by Macrander et al (2005).

The negative salinity anomalies that are passing the Denmark Strait with the East Greenland Current enter the subpolar gyre and reach the Labrador Sea around 2 to 3 years later. Here they cause the Great Salinity Anomaly (GSA) events, which result in a reduction of the vertical ventilation of cold and fresh water (Dickson et al, 1988). After the negative salinity anomalies are passing the Labrador Sea they recirculate further within the subpolar gyre. The most pronounced negative salinity anomaly in the model that passed the Denmark Strait around 1967 can be tracked through their whole pathway in the sub-

polar gyre and needs around $8-9$ years to finally recirculate with the North Atlantic Current (NAC) over the Iceland-Scotland Ridge back to the Greenland Sea. The estimated travel times within the subpolar gyre matches well the propagation time of the 1970s GSA event mentioned by Belkin et al (1998). The modelled 1970s GSA event and to some extent also the GSA events in the early and late 1980s coincides with a high sea ice transport from the Arctic through the Denmark Strait. This agrees with findings of Haak et al (2003), who showed that all GSAs are remotely triggered by abnormal sea-ice and freshwater exports from the Arctic. It is noted that in their model configuration, the surface salinity was restored to climatological values. The GSA events in the early and late 1980s also correspond to an increased sea-ice transport through Davis Strait (not shown) which is in agreement with the findings of (Belkin et al, 1998; Häkkinen, 2002; Belkin, 2004).

The negative temperature and salinity anomalies in the Labrador Sea of the early 1960s and 1990s are both related with an enhanced heat loss in the Labrador Sea due to a strong positive phase of the North Atlantic Oscillation (NAO). This produced cold and dense surface waters which favoured a deep ventilation of cold and fresh water (Yashayaev, 2007; Yashayaev and Loder, 2009). It should be mentioned that because here we use a transient SSS forcing, we can not clearly separate for this model run how much of the GSA events is model skill and how much is related to the salinity forcing. Nevertheless, the comparison of the modelled and observed temperature and salinity time series of van Aken et al (2011), of the 1500 dbar pressure level, which is not directly influenced by the sea surface forcing, reveals that the model is able to reproduce the deep signal of GSA events. An analogous model simulation where the SSS is restored to climatology (not shown) indicates that the model has the skill to also reproduce the surface signal of a GSA event.

The comparison of the the modelled and observational derived March MLD revealed that the model setup is able to reproduce the general location of the main deep water formation areas in the Labrador Sea and Greenland Sea. The the main deep convection area in the model Labrador Sea is slightly shifted to the northwest which could be explained by a lack of eddy induced mixing with the West Greenland Current in the Labrador Sea caused by the limited horizontal resolution as described by Chanut et al (2008). There, the existence of eddies that mix with the warm Irminger Current, the so-called Irminger Rings, can limit the northward extent of the main deep convection area. The modelled maximum MLD is in the range of other ocean model approaches as shown by Griffies et al (2009). In the same time, the observational derived MLD climatology shows a weaker maximum MLD in the Labrador Sea and Greenland Sea. Most of the available data for the Labrador Sea and also Greenland Sea are from late spring to late autumn. So its not fully clear how representative the observed maximum March MLD values are.

The analysis of the modelled and observed WOCE hydrographic section A1E reveals a good agreement in the vertical temperature distribution. The vertical salinity distribution features a pronounced eastward shift of the pathway of the NAC, which can be mainly attributed to the coarser resolution at this

position. Further verified the modelled A1E salinity section, that the model exhibits to fresh DSOW and ISOW water masses.
Our model run features an oscillation between a high and low AMOC phase, where the high AMOC phase is characterized by a strong deep convection in the Labrador- and Greenland Sea, while the low AMOC phase shows a massive drop in the mixed layer depth of these two regions. A waxing and waning of Labrador Sea and Greenland Sea deep convection is documented in observational evidences by several authors (Schlosser et al, 1991; Dickson et al, 1996). CMA of the horizontal temperature and salinity distributions with respect to the maximum AMOC index (not shown) revealed that the positive temperature and salinity anomalies between 44°N-64°N are caused by an increased meridional heat transport and deep convection of the warm and salty North Atlantic waters at the continental slope northwest of the British Isles and southwest of Iceland. The upper cell of the AMOC is connected with the transport of heat and salt into high latitudes, a weakening of this circulation causes a reduction in the heat and salt transport northward. The composite maps (High - Low) of the mean meridional temperature and salinity profile features in the subtropical and middle Atlantic, at $\sim 20^{\circ}$N and a depth of $400 - 800$ m, have a strong negative temperature and salinity anomaly of ~ -0.7 °C and ~ -0.13 psu, respectively. These anomalies are caused by an accumulation of heat and salt in the tropical and subtropical Atlantic during the low AMOC state and the reduced northward transport of heat and salt. The negative temperature anomaly of ~ -0.1 °C between 66°N - 78°N is related to the strong MLD and the associated intensified deep ventilation of cold surface waters in the northern Greenland Sea for the high AMOC phase. For the low AMOC, the MLD in that area is clearly reduced, which reduces the deep ventilation and causes warmer temperatures there.

6 Conclusion

The model setup showed in this paper is able to reproduce large scale features of the ocean circulation and with the ability of locally refined resolution it can simulate the main characteristics of the deep water formation. From the evaluation of our model setup we can summarize:

(1) The sea-ice model produces realistic sea ice concentration on both hemispheres and is able to generate an Arctic sea ice variability as well as a trend in the Southern Ocean sea ice extent that is in agreement with observational data (Schmith and Hansen, 2003; Fetterer et al, 2002, updated 2009).
(2) On the basis of a comparison with OWS data, we could prove that the model setup performs very well in areas with a high resolution.
(3) The model features the fingerprint of several GSA events in the vertical that are documented in observational data by several authors (Dickson et al, 1988; Belkin et al, 1998; Belkin, 2004).

(4) The analysis of the Denmark Strait cross section indicates that the model captures the freshening trend of the last four decades in the North Atlantic as its described by Dickson et al (2002).
(5) The model generally tends to underestimate the strength and salinity of the Nordic Sea overflows, which could be an explanation for the slenderness and weakness of the upper AMOC circulation cell.
(6) We found a pronounced variability in the AMOC which is accompanied by a corresponding fluctuation in the mixed layer of the Labrador Sea and Greenland Sea.

As a logical next step, we will apply our model to different climate conditions. A dedicated study of the deep water formation in the North Atlantic based on the setup validated here will be presented in an upcoming paper.

References

van Aken HM, Jong MF, Yashayaev I (2011) Decadal and multi-decadal variability of Labrador Sea Water in the north-western North Atlantic Ocean derived from tracer distributions: Heat budget, ventilation, and advection. Deep-Sea Research I 58(5):505–523

Balmaseda MA, Smith GC, Haines K, Anderson D, Palmer TN, Vidard A (2007) Historical reconstruction of the Atlantic Meridional Overturning Circulation from the ECMWF operational ocean reanalysis. Geophys Res Lett 34:L23,615

Belkin I (2004) Propagation of the "Great Salinity Anomalies" of the 1990s around the northern North Atlantic. Geophys Res Lett 31:L08,306, DOI 10.1029/2003GL019334

Belkin I, Levitus S, Antonov J, Malmberg S (1998) "Great Salinity Anomalies" in the North Atlantic. Prog Oceanog 41:1–68

Bersch M (1995) On the circulation of the North Atlantic. Deep-Sea Research I 42(9):1583–1607

Bersch M, Meincke J, Sy A (1999) Interannual thermohaline changes in the northern North Atlantic 1991-1996. Deep-Sea Research II 46:55–77

de Boyer Montegut C, Madec G, Fischer AS, Lazar A, Iudicone D (2004) Mixed layer depth over the global ocean: an examination of profile data and a profile-based climatology. J Geophys Res 109:C12,003, DOI 0.1029/2004JC002378

Bromwich DH, Ryan LF, Hodges KI, Walsh JE (2007) A tropospheric assessment of ERA-40, NCEP, JRA-25 global reanalyses in the polar regions. J Geophys Res 112:D10,111

Carton JA, Giese BS (2008) A Reanalysis of Ocean Climate Using Simple Ocean Data Assimilation (SODA). Mon Weather Rev 136:2999–3017

Cavalieri D, Parkinson C, Gloersen P, Zwally HJ (1996, updated 2007) Sea ice concentration from Nimbus-7 SMMR and DMSP SSM/I-SSMIS Passive microwave data, January 1979-June 2006. National Snow and Data Center, Boulder, CO, USA, (Digital Media)

Chanut J, Barnier B, Large W, Debreu L, Penduff T, Molines JM, Mathiot P (2008) Mesoscale Eddies in the Labrador Sea and Their Contributions to Conversion and Restratification. J Phys Oceanogr 38(8):1617–1643

Cunningham SA, Kanzow T, Rayner D, Baringer MO, Johns WE, Marotzke J, Longworth HR, Grant EM, Hirschi JJM, Beal LM, Meinen CS, Bryden HL (2007) Temporal variability of the atlantic meridional overturning circulation at 26.5n. Science 317(5840):935–938, DOI 10.1126/science.1141304

Curry R, Dickson B, I Y (2003) A change in the freshwater balance of the Atlantic Ocean over the past four decades. Nature 426:826–829, DOI 10.1038/nature02206

Danilov S, Kivman G, Schröter J (2004) A finite element ocean model: principles and evaluation. Ocean Modell 6:125–150

Danilov S, Kivman G, Schröter J (2005) Evaluation of an eddy-permitting finite-element ocean model in the North Atlantic. Ocean Modell 10:35–49

Dickson B, Yashayaev I, Meincke J, Turrell B, Dye S, Holfort J (2002) Rapid freshening of the deep North Atlantic Ocean over the past four decades. Nature 416:832–837, DOI 10.1038/416832a

Dickson R, Brown J (1994) The production of North Atlantic deep water: Sources, rates and pathways. J Geophys Res 99:12,319–12,341

Dickson R, Meincke J, Malmberg SA, Lee AJ (1988) The Great Salinity Anomaly in the Northern North Atlantic 1968-1982. Prog Oceanog 20:103–151

Dickson R, Lazier J, Meinicke J, Rhines P, Swift J (1996) Long-term coordinated changes in the convective activity of the North Atlantic. Prog Oceanog 38:241–295

Döscher R, Redler R (1997) The Relative Importance of the Northern Overflow and Subpolar Deep convection for the North Atlantic Thermohaline Circulation. J Phys Oceanogr 25:1894–1901

Edwards MO (1989) Global gridded elevation and bathymetry (ETOPO5), Digital raster data on a 5-minute geographic (lat/lon) 2160'4320 (centroid-registered) grid. NOAA Natl Geophys Data Cent, Boulder, Colo

Eldevik T, Nilsen JEO, Anders Olsson K, Sando AB, Drange H (2009) Observed sources and variability of Nordic seas overflow. Nature Geosci 2(6):406–410

Fetterer F, Knowles K, Meier W, Savoie M (2002, updated 2009) Sea ice index, National Snow and Data Center, Boulder, CO. www.ndsic.org/data/seaice_index/, (Digital Media)

Fix GJ (1975) Finite-Element models for ocean circulation problems. SIAM J Appl Math 29:371–387

Ford R, Pain CC, Goddard AJH, de Oliveira CRE, Umpleby AP (2004) A nonhydrostatic finite-element model for three-dimensional stratified oceanic flows. Part I: Model formulation . Mon Weather Rev 132:2816–2844

Girton JB, Sanford TB (2001) Synoptic sections of the Denmark Strait Overflow. Geophys Res Lett 28(8):1619–1622

Griffies SM, Biastoch A, Böning C, Bryan F, Danabasoglu G, Chassignet EP, England MH, Gerdes R, Haak H, Hallberg RW, Hazeleger W, Jungclaus

J, Large WG, Madec G, Pirani A, Samuels BL, Scheinert M, Gupta AS, Severijns CA, Simmons HL, Treguier AM, Winton M, Yeager S, Yin J (2009) Coordinated Ocean-ice Reference Experiments (COREs). Ocean Modelling 26(1-2):1 – 46, DOI 10.1016/j.ocemod.2008.08.007

Haak H, Jungclaus J, Latif M (2003) Formation and propagation of great salinity anomalies. Geophys Res Lett 30(9):1473, DOI 10.1029/2003GL017065

Häkkinen S (2002) Freshening of the Labrador Sea surface waters in the 1990s: Another great salinity anomaly? Geophys Res Lett 29(24):2232, DOI 10.1029/2002GL015243

Kwok R, Rothrock DA (1999) Variability of Fram Strait ice flux and North Atlantic Oscillation. J Geophys Res 104(C3):5177–5189, DOI 10.1029/1998JC900103

Large WG, Yeager SG (2008) The global climatology of an interannually varying air-sea flux data set. Clim Dyn 32(2):341–364, DOI 10.1007/s00382-008-0441-3

Latif M, Böning C, Willebrand J, Biastoch A, Dengg J, Keenlyside N, Schweckendier U (2006) Is the Thermohaline Circulation Changing ? Geophys Res Lett 19(18):46314637

Lazier JRN (1980) Oceanographic conditions at Ocean Weather Ship Bravo, 1964-1974. Atmosphere-Ocean 18(3):227–238

Levitus S, Antonov JI, Boyer TP (1994) Interannual Variability of Temperature at a Depth of 125 Meters in the North Atlantic Ocean. Science 266:96–99

Lohmann G, Haak HI, Jungclaus JH (2008) Estimating trends of Atlantic meridional overturning circulation from long-term hydrographic data and model simulations. Ocean Dynamics 58:127–138, DOI 10.1007/s10236-008-0136-7

Macrander A, Send U, Valdimarsson H, Jonsson S, Käse RH (2005) Interannual changes in the overflows from the Nordic Seas into Atlantic Ocean through Denmark Strait. Geophys Res Lett 32:L06,606

Macrander A, Käse RH, Send U, Valdimarsson H, Jonsson S (2007) Spatial and temporal structure of the Denmark Strait Overflow revealed by acoustic observations. Ocean Dynamics 57:75–89

Meier W, Fetterer F, Knowles K, Savoie M, Brodzik MJ (2006, updated 2007) Sea ice concentration from Nimbus-7 SMMR and DMSP SSM/I passive microwave data, July-December 2006. National Snow and Data Center, Boulder, CO, USA, (Digital Media)

Meincke J (1991) WHP Cruise Summary Information of section A01E , WOCE. Bremerhaven, PANGAEA

Sarafanov A, Falina A, Mercier H, Lherminier P, Sokov A (2009) Recent changes in the Greenland-Scotland overflow-derived water transport from hydrographic observations in the southern Irminger Sea. Geophys Res Lett 36:L13,606

Schlitzer R (2000) Electronic Atlas of WOCE Hydrographic and Tracer Data Now Available. Eos Trans AGU, 81(5):45

Schlosser P, Bönisch G, Rhein M, Bayer R (1991) Reduction of Deepwater Formation in the Greenland Sea During the 1980s: Evidence from Tracer Data. Science 251:1054–1056

Schmith T, Hansen C (2003) Fram Strait Ice Export during the Nineteenth and Twentieth Centuries Reconstructed from a Multiyear Sea Ice Index from Southwestern Greenland. J Climate 16:2782–2791

Sidorenko D, Danilov S, Wang Q, Huerta-Casas A, Schröter J (2009) On computing transports in finite-element models. Ocean Modelling 28:60–65, DOI 10.1016/j.ocemod.2008.09.001

Sidorenko D, Wang Q, Danilov S, Schröter J (2011) FESOM under coordinated ocean-ice reference experiment forcing. Ocean Dynamics 61:881–890, DOI 10.1007/s10236-011-0406-7

von Storch H, Zwiers FW (2003) Statistical Analysis in Climate Research. Cambridge University Press

Timmermann S R Danilov, Schröter J, Böning C, Sidorenko D, Rollenhagen K (2009) Ocean circulation and sea ice distribution in a finite element global sea ice-ocean model. Ocean Modelling 27:114–129, DOI 10.1016/j.ocemod.2008.10.009

Wang Q, Danilov S, Schröter J (2008a) Comparison of overflow simulations on different vertical grids using the Finite Element Ocean circulation Model. Ocean Modelling 20:313–335, DOI 10.1016/j.ocemod.2007.10.005

Wang Q, Danilov S, Schröter J (2008b) Finite Element Ocean circulation Model based on triangular prismatic elements, with application in studying the effect of topography representation. J Geophys Res 113, DOI 10.1029/2007JC004482

Wang Q, Danilov S, Hellmer HH, Schröter J (2010) Overflow dynamics and bottom water formation in the western Ross Sea: Influence of tides. J Geophys Res 115(1-16), DOI 10.1029/2010JC006189

Wang Q, Myers PG, Hu X, Bush ABG (2012a) Flow Constraints on Pathways through the Canadian Arctic Archipelago. Atmosphere-Ocean 50(3):373–385

Wang X, Wang Q, Sidorenko D, Danilov S, Schröter J, Jung T (2012b) Long term ocean simulation in FESOM: Evaluation and application in studying the impact of Greenland Ice Sheet melting. Ocean Dynamics DOI 10.1007/s10236-012-0572-2

Warren BA, Wunsch C (2007) Deep circulation of the world ocean, in Evolution of physical oceanography, chapter 1. Massachusetts Institute of Technology: MIT Open Course Ware

White L, Deleersnijder E, Legat V (2008a) A three-dimensional unstructured mesh finite element shallow-water model, with application to the flows around an island and in a wind-driven, elongated basin. Ocean Modelling 22:26–47

Yashayaev I (2007) Hydrographic changes in the Labrador Sea, 1960-2005. Prog Oceanog 73:242–276, DOI 10.1016/j.pocean.2007.04.015

Yashayaev I, Loder W (2009) Enhanced production of Labrador Sea Water in 2008. Geophys Res Lett 36, DOI 10.1029/2008GL036162

Zhang R, Delworth TL, Rosati A, Anderson WG, Dixon KW, Lee HC, Zeng F (2011) Sensitivity of the North Atlantic Ocean Circulation to an abrupt change in the Nordic Sea overflow in a high resolution global coupled climate model. J Geophys Res 116:C12,024